FINAL REPORT

Demonstration of Ultrahigh-Strength Nanocrystalline Copper Alloys for Military Applications

SERDP Project WP-2438

JUNE 2015

Kris Darling
U.S. Army Research Laboratory

Distribution Statement A
This document has been cleared for public release

SERDP
DOD ▪ EPA ▪ DOE

REPORT DOCUMENTATION PAGE

Form Approved
OMB No. 0704-0188

The public reporting burden for this collection of information is estimated to average 1 hour per response, including the time for reviewing instructions, searching existing data sources, gathering and maintaining the data needed, and completing and reviewing the collection of information. Send comments regarding this burden estimate or any other aspect of this collection of information, including suggestions for reducing the burden, to Department of Defense, Washington Headquarters Services, Directorate for Information Operations and Reports (0704-0188), 1215 Jefferson Davis Highway, Suite 1204, Arlington, VA 22202-4302. Respondents should be aware that notwithstanding any other provision of law, no person shall be subject to any penalty for failing to comply with a collection of information if it does not display a currently valid OMB control number.
PLEASE DO NOT RETURN YOUR FORM TO THE ABOVE ADDRESS.

1. REPORT DATE *(DD-MM-YYYY)*	2. REPORT TYPE	3. DATES COVERED *(From - To)*
8-25-2015	Final	Aug 2014 -Aug 2015

4. TITLE AND SUBTITLE
Demonstration of Ultrahigh-Strength Nanocrystalline Copper Alloys for Military Applications

5a. CONTRACT NUMBER

5b. GRANT NUMBER

5c. PROGRAM ELEMENT NUMBER

6. AUTHOR(S)
Kris A Darling, Ryan R Carpenter, Anthony Roberts, Chris D Haines and Laszlo J Kecskes

5d. PROJECT NUMBER
WP-2483

5e. TASK NUMBER

5f. WORK UNIT NUMBER

7. PERFORMING ORGANIZATION NAME(S) AND ADDRESS(ES)
U.S. Army Research Laboratory
RDRL-WMM-F
APG, MD 21005

8. PERFORMING ORGANIZATION REPORT NUMBER

9. SPONSORING/MONITORING AGENCY NAME(S) AND ADDRESS(ES)
Strategic Environmental Research and Development Program
901 North Stuart Street, Suite 303
Arlington, VA 22203

10. SPONSOR/MONITOR'S ACRONYM(S)
SERDP

11. SPONSOR/MONITOR'S REPORT NUMBER(S)

12. DISTRIBUTION/AVAILABILITY STATEMENT
Approved for public release; distribution unlimited.

13. SUPPLEMENTARY NOTES

14. ABSTRACT

The objective of this research was to further explore novel alloy development via powder processing synergistically combined with innovative consolidation methodologies to fabricate nanocrystalline Cu-based alloys with thermal stability and properties suitable for substitution of Cu-Be and its applications. Previously, it was also demonstrated that both the mechanical properties as well as the electrical properties of the Cu-Ta alloys can be tailored by changing the Ta content or by changing the temperature used during consolidation to match or exceed the properties of Cu-Be alloys. This past preliminary study did not provide a sufficiently thorough investigation of the chemistry/properties relationship. Therefore, the specific objectives of the current proposed work was to elucidate the processing-nanostructure-property-performance interrelationships in an array of nanocrystalline Cu-Ta alloys through a more systematic investigation of thermo-mechanical processing conditions and alloy composition effects. These scientific studies are to establish and define the property tradeoffs available in this system, and to understand the adjustment range of both physical and mechanical properties.

15. SUBJECT TERMS
Nanocrystalline, Cu-Ta, Cu-Be, powder processing

16. SECURITY CLASSIFICATION OF:			17. LIMITATION OF ABSTRACT	18. NUMBER OF PAGES	19a. NAME OF RESPONSIBLE PERSON
a. REPORT	b. ABSTRACT	c. THIS PAGE			Kris A Darling
UNC	UNC	UNC	UU		19b. TELEPHONE NUMBER *(Include area code)* 410-306-0862

Reset

Standard Form 298 (Rev. 8/98)
Prescribed by ANSI Std. Z39.18

Table of Contents

1. List of Figures ii
2. List of Tables iv
3. List of Acronyms v
4. Key Words vi
5. Acknowledgements vi

6. Abstract 1
7. Introduction 1
- a. Current Status of Cu-Be Alloys 1
- b. Nanocrystalline Metals, A Suitable Alternative Replacement Material? 2
- c. Previous Work 2
- d. Current Project Objectives 2

8. Experimental Methods and Deliverables 3
- a. High Energy Mechanical Alloying 3
  - *i. Laboratory Investigations: Small Scale* 4
  - *ii. Laboratory Investigations: Transition from Small to Large Scale* 4
- b. Associated Challenges and Consolidation of Thermally Stable Powders 4
- c. Consolidation of Thermally Stable Powders 5
  - i. *Equal Channel Angular Extrusion (ECAE)* 5
  - *ii. Instrumented Hot Isostatic Pressing (HIPing)* 6
  - *iii. Field Assisted Sintering Technology (FAST)* 6
- d. Characterization of Alloys 7
  - *i. Transmission Electron Microscopy (TEM)* 7
  - *ii. Scanning Electron Microscopy (SEM)* 7
  - *iii. X-Ray Diffraction Studies* 8
  - *iv. Vickers Microhardness Testing* 8
  - *v. Tension, Compression, and Shear Testing* 8
  - *vi. Machining* 8

9. Results 8
- a. Experimental Results: Small Scale Samples 8
- b. Experimental Results: Acta Materialia Publication 9
- c. Supplementary Work Performed: High Temperature Mechanical Tests 11
- d. Experimental Results: Large Scale Samples 12

10. Conclusions 24
11. References 25
12. Appendix 26

Acta Materialia Publication: entitled "Microstructure and Mechanical Properties of Bulk Nanostructured Cu-Ta Alloys Consolidated by Equal Channel Angular Extrusion," by Darling, KA, Tschopp, MA, Guduru, RK, Yin, WH, Wei, Q, and Kecskes, LJ, Acta Materialia, 76, 168-185, September 2014 27

List of Figures:

Figure 1: Examples of a processed bulk part from Cu-Ta precursor powders fabricated a large-scale Zoz mill and subsequently consolidated via HIP 6

Figure 2: Examples of Cu-Ta powders processed using a Zoz mill and a plate consolidated via FAST 7

Figure 3: Graph of grain growth for Cu-Ta alloys as a function of annealing temperature and Ta concentration, i.e., 1, 5 and 10 at.% Ta in Cu **10**

Figure 4: Graph of Vickers microhardness Cu-Ta alloys as a function of annealing temperature and Ta concentration, i.e., 1, 5, and 10 at.% Ta in Cu **10**

Figure 5: Graph of Vickers microhardness Cu-Ta alloys as a function of ECAE consolidation temperature and Ta concentration, i.e., 1, 5, and 10 at,% Ta in Cu **11**

Figure 6: High temperature quasi-static compressive stress-strain curves for Cu-10Ta 700 °C. OFHC copper compressed at room temperature is provided for comparison to the nanostructured Cu-Ta alloy **12**

Figure 7: Backscatter electron mode scanning electron micrographs of Cu-10Ta as a function of milling time. In the images, the dark gray areas correspond to Cu; and the light gray to white areas correspond to Ta. Note, the size of the white specks get smaller with increasing time, especially at 8 hours **13**

Figure 8: Backscatter electron mode scanning electron micrographs of Cu-5Ta as a function of milling time. Generally, distinct precursor grains of Ta are no longer evident as was in the case of Cu-10Ta; the breakdown follows the same general trend with time **13**

Figure 9: Backscatter electron mode scanning electron micrographs of Cu-1Ta as a function of milling time. Generally, distinct precursor grains of Ta are no longer evident as was in the case of Cu-10Ta and Cu-5Ta; the Ta breakdown follows the same general trend with time **14**

Figure 10: Backscatter electron mode scanning electron micrographs of Cu-10Ta as a function of milling time with and without stearic acid (note, this hydrocarbon is a typical process control agent used to prevent cold welding and increase the level of dispersion.) at increasing magnifications; top row: with stearic acid; and bottom row: without stearic acid **15**

Figure 11: X-ray diffraction patterns as a function of milling time for the as-milled Cu-1 at.% Ta powder. All peaks show extensive broadening and well as a shift in both Cu and Ta peak positions. Additionally, observe the non-symmetrical shoulder broadening **18**

Figure 12: X-ray diffraction patterns as a function of milling time for the as-milled Cu-5 at.% Ta powder. The primary Ta peaks are observed to shift to lower scattering angles indicating alloy

formation between Ta and Cu. All peaks show extensive broadening. Additionally, observe the non-symmetrical shoulder broadening..... **18**

Figure 13: X-ray diffraction patterns as a function of milling time for the as-milled Cu-10 at.% Ta powders. The primary Ta peaks are observed to strongly shift to lower angles indicating significant alloy formation between Cu and Ta. Additionally, all peaks show extensive broadening..... **19**

Figure 14: Backscatter electron mode scanning electron micrographs of the HIP consolidated Cu-Ta samples as a function of Ta concentration; 1, 5, and 10 at.% Ta. In the images, the dark gray areas correspond to Cu; and the light gray areas correspond to Ta. Once consolidated, increasing the Ta content results in a higher density of Ta particles. The images did not reveal the presence of porosity **21**

Figure 15: Backscatter electron mode scanning electron micrographs of fracture surfaces from the HIP consolidated Cu-Ta samples as a function of Ta concentration; 1, 5, and 10 at.% Ta. In the images, the dark gray areas correspond to Cu; and the light gray areas correspond to Ta. Note, larger Ta particles appear to be the nucleation sites for the formation of microvoids..... **22**

Figure 16: Tension ductility of the ECAE consolidated Cu-1Ta and Cu-10Ta samples, processed at various temperatures. Note the rapid drop in strenght and commensurate increase in ductility of the samples. **2**3

Figure 17: Macrophotographs of Cu-Ta alloy parts. The displays show near-net shaped conical and hemispherical geometries produced by instrumented HIPing of Cu-1Ta (cones) and Cu-10Ta (hemisphere). Note, the exterior surface of the hemispherical dome has been machined..... **2**4

List of Tables:

Table 1: Data shows the results of trace chemical analysis of the as-milled Cu-Ta powders as a function of milling time. The composition of the alloys tested were 1, 5, and 10 at.% Ta, respectively. The red box highlights the Fe results; the increasing levels arise from the milling chamber and grinding media..... **16**

Table 2: Oxygen impurity pick-up during the milling of the Cu-Ta powders with 1, 5, and 10 at.% Ta levels as a function of milling time. **17**

Table 3: Reduction of Cu grain size and Ta particle size as a function of milling time. The respective grain and particles size values agree well with those observed in the earlier small scale studies **20**

1. List of Acronyms:

ABD: Acute Beryllium Disease
ACGIH: American Conference of Governmental Industrial Hygienists
ARDEC: Armament Research, Development and Engineering Center
ARL: Army Research Lab
ASTM: American Society for Testing and Materials
CAMPS: ARL Center for Advanced Metals Powder Synthesis
CBD: Chronic Beryllium Disease
DOD: Department of Defense
DOE: Department of Energy
DSC: Differential Scanning Calorimetry
ECAE: Equal Channel Angular Extrusion
EDS: Energy Dispersive Spectroscopy
EELS: Electron Energy Loss Spectroscopy
ESTCP: Environmental Security Technology Certification Program
FAST: Field Assisted Sintering Technology
FIB: Focused Ion Beam
GB: Grain Boundary
GS: Grain Size
HP: Hot Pressing
HIP: Hot Isostatic Pressing
IACS: International Annealed Copper Standard
IARC: International Agency for Research on Cancer
ISO: International Organization for Standardization
MA: Mechanical Alloying
MA: Mechanical Alloying
MPa: Megapascal
MWM: Meandering Winding Magnetometer
OFHC: Oxygen Free High Conductivity
OSHA: Occupational Safety and Health Administration
PCA: Process Control Agent
PLS: Pressure-Less Sintering
PMNTC: ARDEC Powder Metallurgy and Nano Technology Center
SEM: Scanning Electron Microscope/Microscopy
SERDP: Strategic Environmental Research and Development Program
SPD: Severe Plastic Deformation
SPS: Spark Plasma Sintering
STEM: Scanning Transmission Electron Microscope/Microscopy
TEM: Transmission Electron Microscope/Microscopy
UTS: Ultimate Tensile Strength
USNRC: United States National Research Council
YS: Yield Strength
XRD: X-Ray Diffraction

2. Key Words:

Cu-Be Replacement, Nanocrystalline, Cu-Ta, Copper Beryllium, Copper Tantalum, Powder Processing

3. Acknowledgements:

The development of these Cu-Ta alloys was accomplished with assistance from the following individuals:

Mr. Anthony Roberts of the U.S. Army Research Laboratory
Mr. Joseph Paras of the Army RDCOM-ARDEC, Picatinny Arsenal, NJ
Mr. Ryan Carpenter of the Army RDCOM-ARDEC, Picatinny Arsenal, NJ
Dr. Christopher Haines of the Army RDCOM-ARDEC, Picatinny Arsenal, NJ
Dr. Tony Zahrah of MATSYS Corporation, Sterling VA
Mr. Micah Gallagher of the U.S. Army Research Laboratory
Professor Yuri Mishin of George Mason University
Mr. Deepak Kapoor of the Army RDCOM-ARDEC, Picatinny Arsenal, NJ
Mr. Bradley Klotz of the U.S. Army Research Laboratory
Mr. James Catalano of the U.S. Army Research Laboratory
Professor Qiuming Wei, University of North Carolina at Charlotte

4. Abstract:

The objective of this research was to further explore novel alloy development via powder processing synergistically combined with innovative consolidation methodologies to fabricate nanocrystalline Cu-based alloys with thermal stability and properties suitable for substitution of Cu-Be and its applications. Previously, it was also demonstrated that both the mechanical properties as well as the electrical properties of the Cu-Ta alloys can be tailored by changing the Ta content or by changing the temperature used during consolidation to match or exceed the properties of Cu-Be alloys. This past preliminary study did not provide a sufficiently thorough investigation of the chemistry/properties relationship. Therefore, the specific objectives of the current proposed work was to elucidate the processing-nanostructure-property-performance interrelationships in an array of nanocrystalline Cu-Ta alloys through a more systematic investigation of thermo-mechanical processing conditions and alloy composition effects. These scientific studies are to establish and define the property tradeoffs available in this system, and to understand the adjustment range of both physical and mechanical properties.

5. Introduction:

a. Current Status of Cu-Be Alloys

The dermatological, pulmonary, and systemic toxicity of beryllium (Be) and Be-containing alloys has been known for over 70 years [1] and has been linked to a number of severe industrial health issues in the United States. Furthermore, the International Agency for Research on Cancer (IARC) lists Be as a Category 1 Carcinogen. While the Occupational Safety and Health Administration (OSHA), US Department of Energy (DOE) and the American Conference of Governmental Industrial Hygienists (ACGIH) have recommended that the acceptable exposure limit be lowered by as much as a 40 times [2], the United States National Research Council (USNRC) has recommended that Be exposure be limited to "the lowest feasible level," as the agency's research could not establish any safe level of exposure [2].http://en.wikipedia.org/wiki/Beryllium - cite_note-38#cite_note-38

The largest US utilization of Be is in Be-containing alloys of which copper-Be (Cu-Be) alloys are the most ubiquitous form. Recent studies have shown that even Cu-alloys containing less than 4% Be have been linked to causing chronic beryllium disease (CBD), making them just as hazardous as pure Be metal [3-4]. The development of alternative Cu alloys with similar or greater physical properties without the adverse ecological and toxicological effects would therefore greatly reduce the health risks, liability and long term costs associated with manufacturing.

The main difficulty in replacing Cu-Be alloys lies in their outstanding combination of physical properties. The addition of 2 wt.% Be can increase the strength of Cu six-fold. After precipitation hardening, these alloys are capable of achieving a tensile strength of 174 ksi (1200 MPa) while retaining a reasonable amount of ductility (~5%) [5-6]. This outstanding versatility, leads to exceptional performance and manufacturability which **to date has not been matched by**

alternative alloys, most specifically at the highest strength most extreme physical properties. Therefore, despite the horrific health risks from exposure during manufacturing the use and demand for these toxic alloys still persists.

b. Nanocrystalline Metals, a Suitable Alternative Replacement Material?

In recent years, nanocrystalline metals and alloys have had the attention of the scientific community. This is mainly due to the intriguing mechanical properties with which they are associated. Numerous reports now exist, indicating an order of magnitude increase in strength is possible in metals and alloys that exhibit grain sizes approaching the lower limit of nanocrystallinity [7-10]. While achieving high strength has never been a problem, the ability to achieve any amount of uniform elongation, the prerequisite for appreciable ductility, was a challenge in the past [11-13]. Recently, numerous reports of improved ductility indicate that tens of percent elongation may be possible in nanocrystalline metals [14-16]. The combination of ultra high strength and improved ductility of nanocrystalline metals makes what was impossible in the past, possible today, such as the replacement of Cu-Be alloys. However, as indicated by thermodynamic principles, nanocrystalline microstructures in metals are subject to coarsening at elevated temperatures [17-22]. The result of such nano-to-micro scale coarsening is the loss of the remarkable physical properties and deformation behaviors associated with these microstructures. This inherent thermal instability frequently limits the overall processing and applications of nanocrystalline metals. That is, nanocrystalline materials would benefit from thermal stabilization, which, in turn, would aid real world applications.

c. Previous Work

Under a prior SERDP SEED program, #2139, the successful demonstration and implementation of fabrication protocols for stable bulk nanocrystalline Cu-Ta alloys were accomplished. It was shown that property values in a Cu-Ta alloy, specifically, Cu with 10at.% Ta *can approach or exceed those of Cu-Be alloys even at the highest limit*. Specifically, the objectives were to develop a non-Be containing alloy with an ultimate tensile strength (UTS) of 165 ksi (1138 MPa), yield strength (YS) of 140 ksi (965 MPa), and a Rockwell C hardness of 36-45. The accomplishments of that work produced a thermally-stable, nanocrystalline Cu-10 at.% Ta alloy, exhibiting a UTS of 1300 MPa, YS of 1100 MPa, and Rockwell C hardness of 49 [see final report], thus exceeding the required metrics. The project further incorporated computational simulations [23], demonstrated wear test comparisons with other structural materials, and examined the feasibility of scale-up potential. While these preliminary results were promising, there were a number of other areas that were needed to be investigated, including alloy composition and grain size variation for optimization of increased strength and deformation, as well as determination other physical properties, such as formability at high temperatures or machinability.

d. Current Project Objectives

Under the current SERDP funded project there were two main objectives for the proposed work. The first was to elucidate the processing-nanostructure-property-performance

interrelationships in an array of non-toxic nanocrystalline Cu-Ta alloy compositions which are capable of meeting and exceeding the key characteristics of Cu-Be alloys through a systematic investigation of thermo-mechanical processing conditions and alloy composition effects. These studies were meant to establish the property space available in this system, and to understand the adjustability range of both physical and mechanical properties. The second was to establish the critical steps and protocols to ready the transition of this materials technology to the next level towards a viable commercialization.

Based on the fundamental scientific research and advanced development proposed herein, it is anticipated that the property space attainable for the scale-up potential of nanocrystalline Cu-Ta alloys will be mapped out. The determination of the relevant properties and supporting processing methodologies will result in a tangible technological achievement. In turn, functional work pieces of technological scale and relevance will open up many opportunities for transition for further manufacturing development for specific components of interest. Preliminary discussions and interactions are underway with the Stryker Program Manager Office and US Navy. Efforts will be made to engage other interested organizations for potential insertion of the nanostructured Cu-Ta materials into service. The intellectual property related to the Cu-Ta composite has been protected: a composition-of-matter patent application and another describing the consolidation of powder into bulk parts have been submitted to the USPTO.

8. Experimental Methods and Deliverables:

a. High Energy Mechanical Alloying

Mechanical alloying is an extremely versatile method for producing nanocrystalline metal and alloyed powders. In general, mechanical milling/alloying produces nanostructured materials with grain sizes <<100 nm by the mechanical attrition of coarser-grained precursors. There are primarily three reasons why mechanical alloying was selected for production of the alloys proposed here over other methods. Firstly, most metals/alloys can be prepared through mechanical-alloying with the product being in particulate form. In instances where materials are too ductile to be directly milled into fine powder, e.g., Cu, surfactants and/or cryogenic milling may be used to induce the production of powder. Fine particulates offer greater versatility when considering up-scaling to industrial manufacturing. This is due to the ability for these particulates to be sintered into almost any shape or size given the proper conditions (high temperatures and pressures) and has been in practice in a manufacturing environment. Secondly, high-energy ball milling has been shown to vastly increase the limit of solid solubility in many metallic systems in which equilibrium room temperature solubility does not otherwise exist. This is important for means of controlling the stability of the system, by both kinetic and thermodynamic methods. Thirdly, high-energy ball milling is known to dramatically reduce the grain size in metallic systems to less than 10 nm which is not possible in other severe plastic deformation processes.

i. Laboratory Investigations: Small Scale

As accomplished in the original SERDP SEED funded project, alloy development and initial processing to expand the compositional range of Ta in Cu and its effect on mechanical and physical properties began at ARL's Center for Advanced Metals Powder Synthesis (CAMPS) at Aberdeen Proving Ground. ARL's unique infrastructure allows for the rapid development and prototyping of advanced nanocrystalline metals and alloys. The center is equipped with a number of low volume high-energy processing equipment including mills, which operate at room temperature, subzero, or cryogenic temperatures, and/or operate in an inert atmosphere (low concentrations of O_2 and H_2O). Additionally, CAMPS has access to a wide range of characterization, consolidation, mechanical and physical testing equipment (will be discussed and outlined in subsequent sections).

Deliverable and Milestone 1 (Q4): production of a compositional range of alloys which will exhibit tailored properties, spanning and extending the entire range covered by current Cu-Be alloys.

ii. Laboratory Investigations: Transition from Small to Large Scale

Once analysis of the effect of Ta concentration on the mechanical and physical properties was completed, powder processing was transitioned from a high-energy SPEX alloying process which produced a few grams a day (performed at CAMPS) to a more commercially viable high-energy Zoz milling process at ARDEC's Powder Metallurgy and Nano Technology Center (PMNTC) at Picatinny Arsenal. This transfer to a larger-scale powder production was already accomplished during the SEED program, however, for only one composition (10 at.% Ta in Cu). For the current proposal, 1 at.% Ta was selected for production of similar sized parts for comparison with samples manufactured in the same manner as for the Cu 10 at.% Ta. Based on our experience with the scale up at 10 at.% Ta, we felt that another composition, with a lower atomic fraction of Ta, will allow bracketing the property range of all Cu-Ta alloys, whereby the necessary steps and conditions for transition into the manufacturing environment could be identified.

Deliverable 2 and Milestone 2 (Q4): scaled-up powder production capability at PMNTC of Cu with 1 at.% Ta.

b. Associated Challenges and Consolidation of Thermally Stable Powders

The unprecedented material properties predicted by the Hall-Petch relationship generated a push to produce finer and finer grain sizes and structures over the past five decades. Within recent years, a great deal of work has focused on the practical issues of producing nanocrystalline powders. However, the development of functional engineering components requires that these nanostructures to be consolidated into fully dense macroscopic scale bulk structures. Many researchers have reported on the enhanced sintering characteristics of nanostructured materials [24-25] which allow high densities to be achieved at much lower temperatures than their coarse-grained counterparts. Equation 1 describes a multi-stage sintering

model developed by Johnson et al.[26] that relates the density normalized rate of densification of the specimen ($d\rho/\rho dt$) to the grain size (G).

$$-\frac{d\rho}{3\rho dt} = \frac{\gamma\Omega}{kT}\left(\frac{\Gamma_V D_V}{G^3} + \frac{\Gamma_b \delta D_b}{G^4}\right) \tag{1}$$

where γ is the surface tension, Ω is the atomic volume, k is Boltzmann's constant, T is the absolute temperature, Γ_v and Γ_b are density dependent constants that describe the microstructure, and δ is the grain boundary thickness. As described above, reducing the grain size of the sample can increase the densification rate exponentially. Unfortunately, both grain growth and densification are driven by the same diffusion-based mechanisms. Therefore, the thermal instabilities that lead to an enhanced densification rate also increase the rate of grain growth in this material and the microstructure of the material after sintering is no longer nanocrystalline. The decoupling of grain growth and densification is critical for producing bulk specimens which are necessary for most engineering applications [27].

c. Consolidation of Thermally Stable Powders

Microstructures that exhibit thermal stability in their grain structure also tend to exhibit a similar stability for their particle structure. Sintering is a process that depends on the reduction of energy from the high-energy state of the finely divided powder to the lower energy of the fully consolidated product. Much of the driving force that leads to densification is based on the overall reduction in surface area. Thermodynamically stable nanomaterials are created by reducing the grain boundary and surface energies so that they are essentially in the same state as those of the bulk material. Therefore, the driving force for densification is reduced in the same manner as how the driving force for grain growth is inhibited. When examining Equation 1, note that the microstructural scaling and surface energy terms are highly dependent on the interfacial energies associated with the system and, thus, directly influence the densification behavior of the material.

Although the thermal stability of these materials tends to inhibit the sinterability of nanostructured materials under conventional conditions, improvements in thermal stability open a regime of processing conditions that allow full densification and the retention of a nanocrystalline structure for more novel consolidation approaches. In particular, the application of external pressure during the sintering process, as practiced in HIPing or a combination of pressure and shear, as demonstrated by Equal Channel Angular Extrusion (ECAE), can greatly improve the tendency for densification. ECAE and Field Assisted Sintering Technology (FAST) were shown under the previous SEED funding to be successful densification methods. However, under this project instrumented Hot Isostatic Pressing (HIPing) will be explored, as it is more in line with standard consolidation methods utilized in an industrial manufacturing settings.

i. Equal Channel Angular Extrusion (ECAE)

The ECAE process subjects a billet to high shear around an "L" shaped channel. ECAE can be performed at elevated temperatures for any number of passes and the billet can be rotated

between passes to provide precise texture control for the material. This method, which induces severe plastic deformation (SPD) at elevated temperatures, has demonstrated its effectiveness in consolidating powders that have a very narrow processing window and cannot be easily consolidated using conventional methods such as high hardness, brittle metallic glass powders. In addition, we have applied and shown in the previous SEED funded program the utility of ECAE by consolidating nanocrystalline Cu with 1 and 10 at.% Ta to 100% theoretical density, with just a few passes. The addition of high shear can significantly reduce the temperature required to achieve full density and allow the consolidation of metastable microstructures [28]. Another benefit of this method is that the material samples retain the same basic geometry and cross-section as the starting piece, thus, allowing for relatively simple scale-up. Consolidation strategies at CAMPS focused on ECAE processing to produce small scale rods 0.5-in diameter and less than 4-in long.

Figure 1: Examples of a processed bulk part from Cu-Ta precursor powders fabricated a large-scale Zoz mill and subsequently consolidated via HIP.

ii. Instrumented Hot Isostatic Pressing (HIPing)

In the HIPing process, powders are loaded into cylindrical steel cans and compacted under isostatic pressure at elevated temperatures. The application of the isostatic pressure allows for a more uniform densification and the production of near net shaped parts. Densification is achieved through a combination of plastic deformation, creep and diffusion bonding. The part geometries that can be achieved by this process are only limited by the die geometry/strength and are designed with the specific application in mind. For our project, instrumented HIPing was utilized to produce near net shaped, axisymmetric parts having hemispherical and cone-shaped geometries with several inches in dimension. The instrumentation entailed the use of a specially designed in-situ eddy current sensor that informed the operator when the part reached its minimum diameter or maximum densification for a given HIP pressure and temperature.

iii. Field Assisted Sintering Technology (FAST)

In the FAST process, powders are loaded into graphite dies and compacted under uniaxial pressure and, upon the application of a large electric current flowing through the die and its contents, via Joule heating. The primary benefit of FAST is the drastically reduced sintering times stemming from Joule heating. Specifically, the application of a high current causes rapid volumetric heating at powder particle-particle contacts, resulting in heating of the entire mass from the inside out.

The FAST process typically yields bulk parts in simple geometries such as round or square plates. PMNTC, however, is exploring the use of complex die designs for the purpose of near-net-shaping bulk parts. The intent of near-net-shaping is to minimize material waste in machining operations – consolidating the powder as close as possible to the final dimensions. The part geometries that can be achieved are only limited by the die geometry/strength and will need to be designed for a specific application. PMNTC currently has die sets capable of producing flat plates (round or square), contoured plates (designed for explosively formed penetrators), and hemispherical domes.

Deliverable 3 and Milestone 2 (Q8): production of fully consolidated parts having properties equal to or greater than current Cu-Be alloys and with cm-scale dimensions for compositions containing 1 at.% Ta.

d. Characterization of Alloys

i. Transmission Electron Microscopy (TEM)

The available instrumentation at CAMPS includes a JEM-2100F equipped with scanning transmission electron microscopy (STEM), and energy dispersive x-ray spectroscopy (EDS) capabilities and a FEI Nova 600 a focused-ion-beam (FIB) and scanning electron microscope (SEM). The functionality of one machine equipped with a 17 kV STEM and EDS allows for unprecedented characterization. These equipments were utilized for measuring the average grain size and precipitated phases, if any, as a function of annealing temperature.

Samples will be prepared using an in-situ lift out method using a dual-beam focused ion beam scanning electron microscope (FIB/SEM) [29]. In-situ sample preparation is capable of producing site specific samples with few artifacts resulting from the preparation process and can easily identify microstructures of bulk materials and interfaces for this specific alloy system.

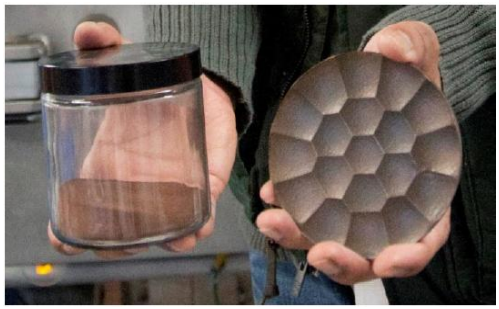

Figure 2: Examples of Cu-Ta powders processed using a Zoz mill and a plate consolidated via FAST.

ii. Scanning Electron Microscopy (SEM)

SEM imaging of the samples was accomplished using a Hitachi S-4700 equipped with an EDS detector. SEM analysis was used to determine the spatial distribution and chemistry of

phases, investigate hardness indentations, characterize residual porosity, and image fracture surfaces of tested samples.

iii. X-Ray Diffraction Studies

X-ray diffraction of the ball-milled and annealed powders, as well as the bulk consolidated pieces were performed with an X'Pert PRO PANalytical MPD x-ray diffractometer using CuKα (λ = 0.1542 nm) radiation. Experimentation allowed data to be collected from as-milled grain size, heat treated, and bulk-consolidated samples, as well as identifying secondary phases, if any, which formed upon processing. Additionally, high temperature X-ray diffraction studies were performed to study grain-growth kinetics.

iv. Vickers Microhardness Testing

Tests were performed on ISO 9000 certified equipment, using ASTM standard operating procedures. Vickers microhardness was used to determine the mean hardness associated with the as-milled powder, heat treated samples, and post-consolidation processed samples (FAST and ECAE).

v. Tension, Compression, and Shear Testing

Tests were performed as to ascertain the mechanical properties including: yield and ultimate strength, ductility and toughness as a function of temperature. These tests were also conducted at various strain rates, including conventional strain rates on the order of 1×10^{-4}. Additionally, for compression testing, strain rates also included high strain rates on the order of 3 to 6×10^{3}, using a Kolsky bar (or Split-Hopkinson pressure bar) apparatus.

vi. Machining

Machinability of the composite was assessed by the direct machining of as-consolidated parts under various materials removal rates and tool speeds and subsequent examination of the freshly cut surfaces. Weldability of the composite was investigated using friction stir welding; specifically, both butt and lap joint geometries were considered. It was expected that a solid-state welding procedure would be more likely to retain and preserve the nanoscale substructure of the Cu-Ta alloys.

9. <u>Results:</u>

a. Experimental Results: Small Scale Samples

Cryogenic milling produced a nanocrystalline Ta-precipitate enriched Cu-rich matrix composite. Scherrer grain size (GS) estimates of the microstructure length scale suggested that the mean GS of the Cu matrix was approximately 10nm for the alloy concentrations examined, specifically, 1, 5 or 10 at.%Ta (the balance being Cu). Figure 1 reflects the thermal stability,

grain size versus Ta content, for the aforementioned alloys; note in the figure that all three alloy compositions display extreme but similar grain size stabilities with increasing temperature. Further insight is provided by the level of microhardness retained as a function of annealing temperature, see Figure 2. In this figure, note the distinct differences that can be observed between these alloys. It is apparent that even when subjected to extreme temperatures nearing the melting point of Cu, the very high hardness values are still retained. Based on these results, exemplary parts displayed in Figures 1 and 2, a study, focusing on comparing the ECAE consolidation temperature to the retained hardness for two alloys, Cu containing 1 and 10 at.%Ta, was conducted. Figure 3 provides the hardness post ECAE processing for various consolidation temperatures. It can be seen that the additional pressure and shear deformation during consolidation has only a moderate effect on decreasing the hardness relative to the isothermal annealing studies as was shown in Figure 2.

Utilizing the data presented in Figure 3, an in-depth analysis was performed on the compositions of Cu containing 1 and 10 at.% Ta, both microstructurally and mechanically for a series of ECAE consolidation temperatures. The selection was based on the noted differences of composition and the corresponding microhardness values, especially at lower temperatures, as assessed from Figure 3.

b. Experimental Results: Acta Materialia Publication

The results of the composition dependent mechanical and microstructural properties of the ECAE processed Cu-Ta alloys have been published in a recent article entitled **"**Microstructure and Mechanical Properties of Bulk Nanostructured Cu-Ta Alloys Consolidated by Equal Channel Angular Extrusion," by Darling, KA, Tschopp, MA, Guduru, RK, Yin, WH, Wei, Q, and Kecskes, LJ, Acta Materialia, 76, 168-185, September 2014. The paper in its entirety is provided in the Appendix of this report; this work clearly identifies and reveals the relevant processing- microstructural-performance relationships of nanostructured Cu-Ta alloys, especially as they relate to the upscaling of processing and fabrication of bulk parts.

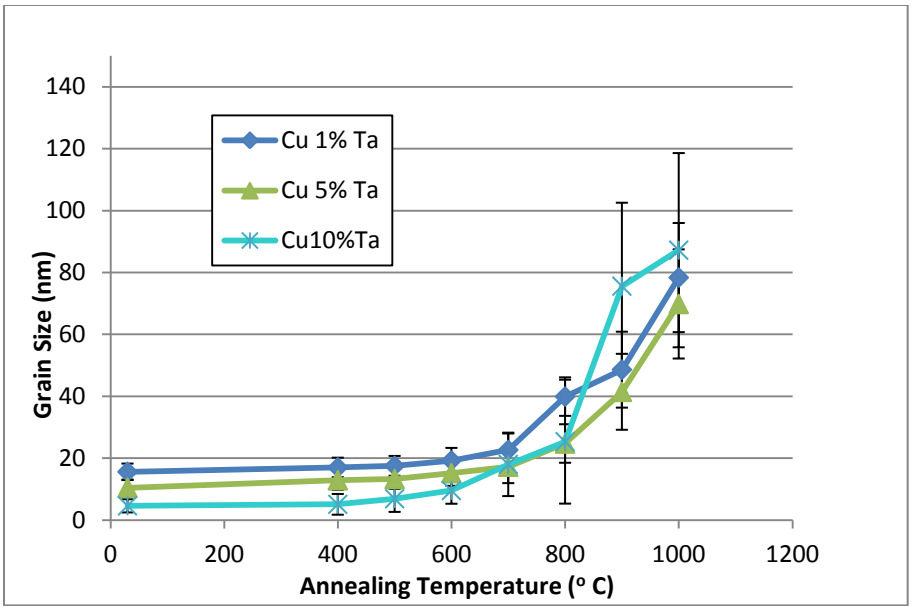

Figure 3: Graph of grain growth for Cu-Ta alloys as a function of annealing temperature and Ta concentration, i.e., 1, 5, and 10 at.% Ta in Cu.

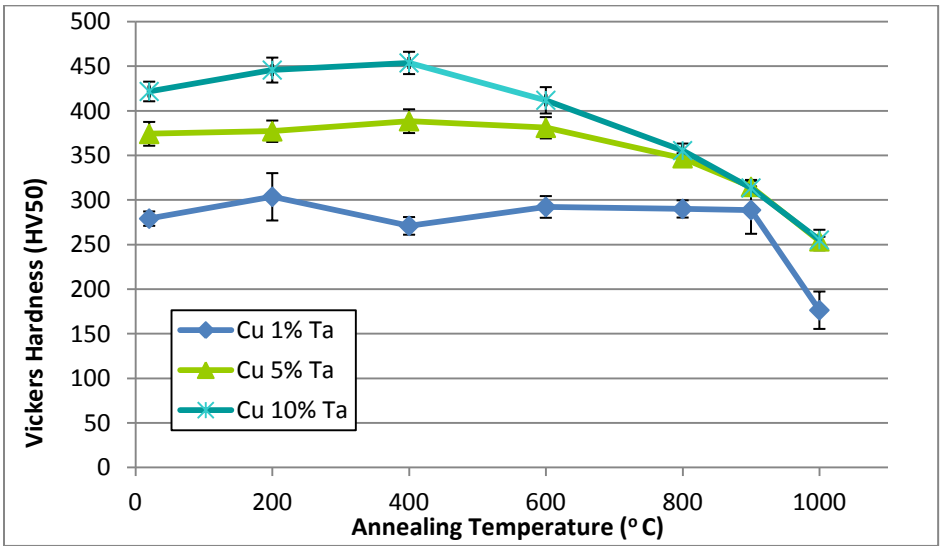

Figure 4: Graph of Vickers microhardness Cu-Ta alloys as a function of annealing temperature and Ta concentration, i.e. 1, 5, and 10 at.% Ta in Cu.

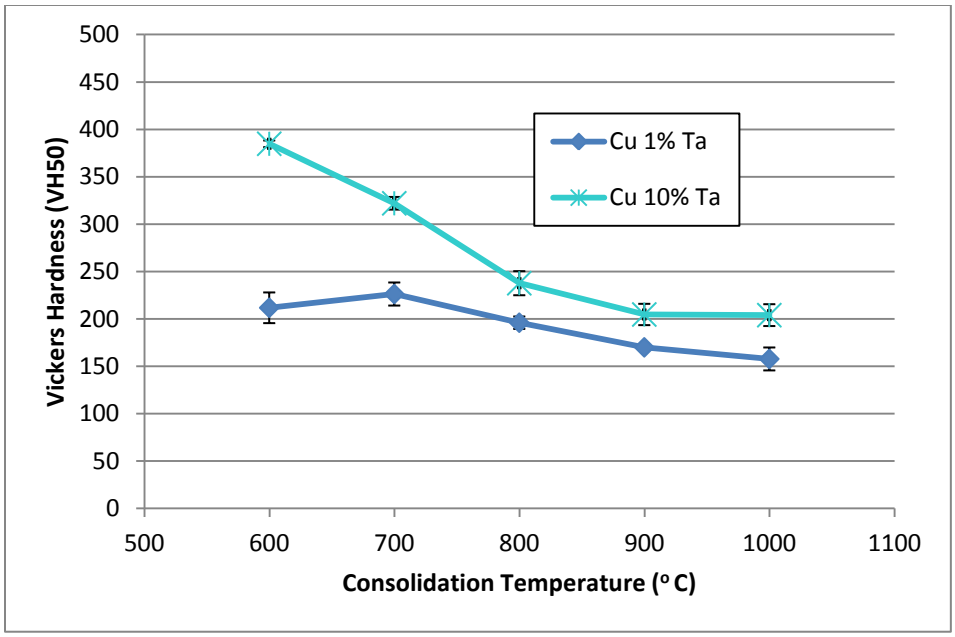

Figure 5: Graph of Vickers hardness Cu-Ta alloys as a function of ECAE consolidation temperature and Ta concentration, i.e. 1, 5, and 10 at.% Ta in Cu.

c. Supplementary Work Performed: High Temperature Mechanical Tests

To investigate the increasing susceptibility and the degree of thermal softening, the ECAE processed Cu-Ta samples were subjected to quasi-static compression tests at high temperatures; the stress-strain curves are provided in Figure 6. As shown, the ultimate flow stress for Cu-10Ta 700 °C at room temperature (curve #1), is approximately 1160 MPa. The corresponding yield strength value is only slightly less, 1050 MPa. This mechanical strength is extremely high, a factor two times that predicted by Hall-Petch strengthening estimates for pure nanocrystalline Cu of the same grain size. The exhibited flow stress is a strong function of the testing temperature and there is a significant contrast to the behavior of coarse-grained copper (dotted line); the reported stress-strain curves for the Cu-Ta samples exhibit an elastic-nearly perfectly plastic behavior. That being the case, past the yield point, the amount of strain hardening is very minor. The lack of strain hardening is particularly evident at higher temperatures, see curves #2 - #7. Note, in some cases, the slopes of the stress strain curves become slightly negative. Additionally, excluding the room temperature curve, all samples demonstrated a smooth and continuous plastic flow with no signs of failure. This indicates that the Cu-Ta alloys have very good high temperature formability. An interesting feature of thermally stabilized nanostructured materials, i.e., the retention of the nanograined microstructure upon cooling, is exhibited by the Cu-Ta alloys as even after testing at 1000°C, a large majority of the room temperature strength was retained.

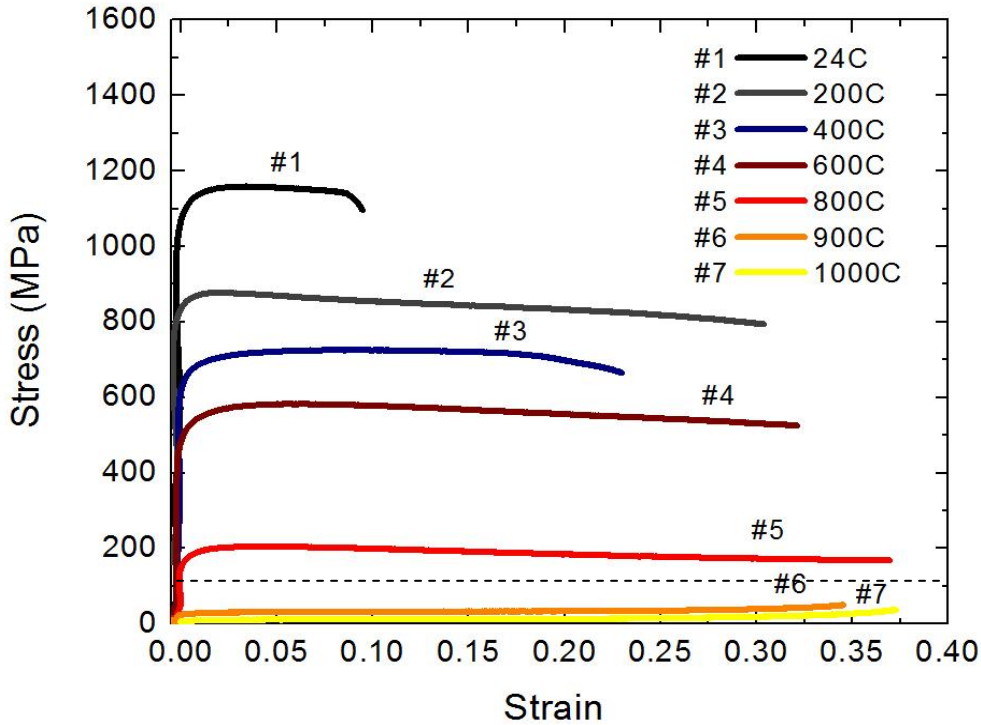

Figure 6: High temperature quasi-static compressive stress-strain curves for Cu-10Ta 700 °C. Well annealed OFHC copper compressed at room temperature (dashed line) is provided for comparison to the nanostructured Cu-Ta alloy.

d. Experimental Results: Large Scale Samples

The large scale production of Cu-Ta alloy powders was accomplished using a CM08 mill purchased from Zoz GmbH, installed and operated at PMNTC. A comprehensive experimental milling program was designed and conducted to investigate the issues associated with scale up and milling kinetics which would occur when utilizing this large capacity mill for the production of significantly larger quantities of nanocrystalline Cu-Ta powder with 1, 5, and 10 at.% Ta concentrations compared to those produced in the much smaller SPEX mill used for the earlier seminal studies. First, 200 g batches were produced as a function of time to investigate the dispersion rate of the Ta metal. Composite images displaying the level of distribution and comminution achieved for a typical Cu-Ta alloy composition from the study are shown in Figure 7. In the figure, starting from left to right, for 1 hour, followed by 2, 4, 6, and 8 hour milling times, the images, collected from representative regions at increasing magnification, reveal that for Cu-10Ta, the level of dispersion between Cu and Ta improves to the point where only a small sub-micrometer Ta particles remain. In comparison, in Figure 8, for Cu-5Ta, at 4, 6, and 8 hour milling times, show much smaller amounts of residual Ta, remaining specifically at shorter time intervals. A similar trend is observed in Figure 9 for Cu-1Ta. In general, then it may be concluded that this series of experiments demonstrates that high-energy Zoz milling is capable of achieving a high dispersion of Ta in a Cu matrix, analogous to what was observed in the small scale milling studies, using high energy SPEX milling operations.

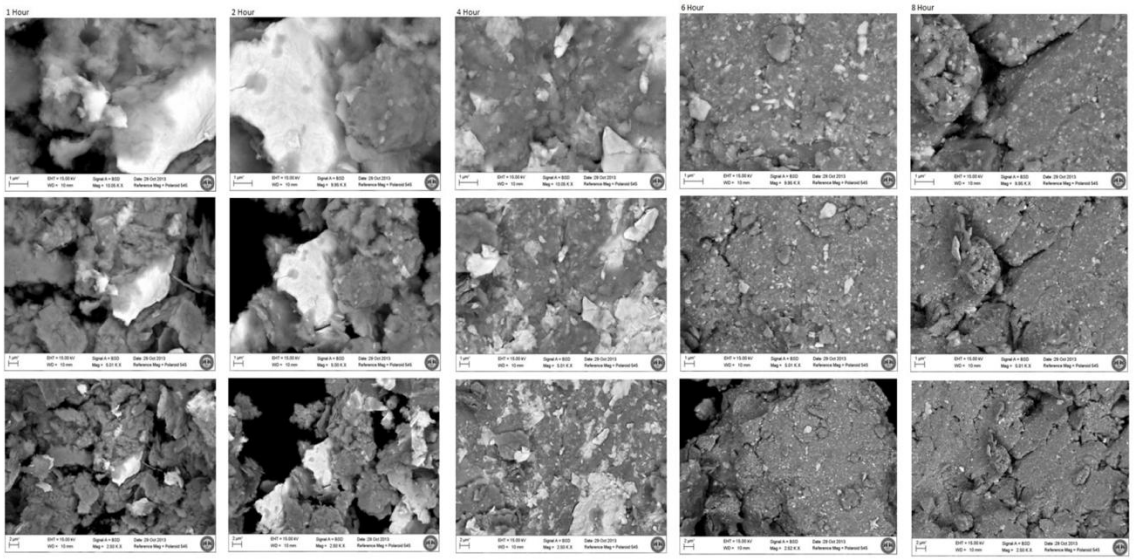

Figure 7: Backscatter electron mode scanning electron micrographs of Cu-10Ta as a function of milling time. In the images, the dark gray areas correspond to Cu; and the light gray to white areas correspond to Ta. Note, the size of the white specks get smaller with increasing time, especially at 8 hours.

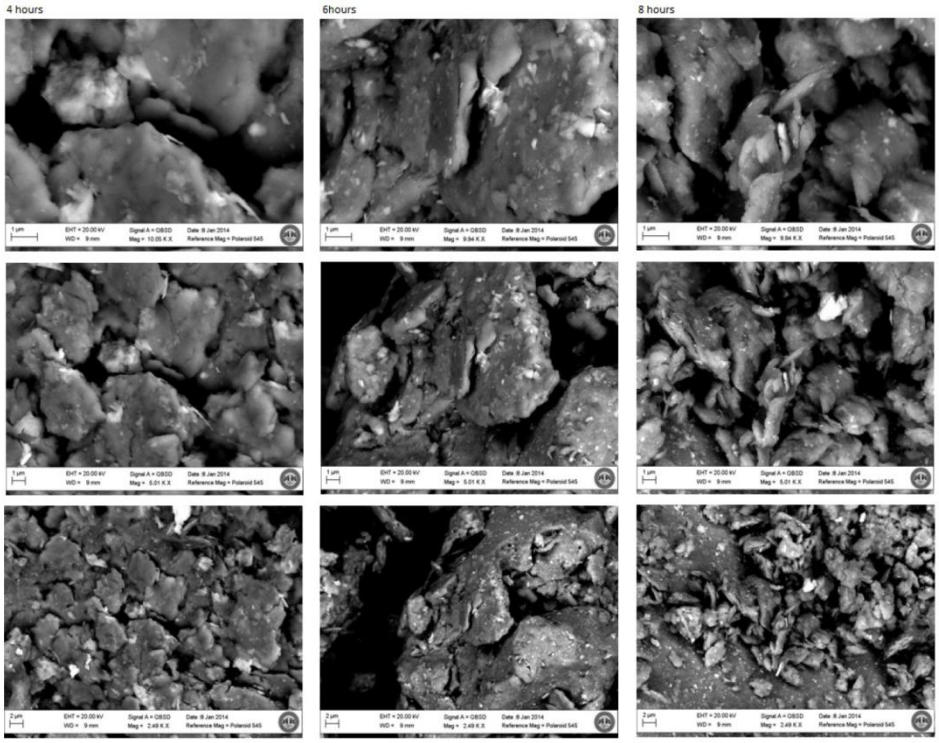

Figure 8: Backscatter electron mode scanning electron micrographs of Cu-5Ta as a function of milling time. Generally, distinct precursor grains of Ta are no longer evident as was in the case of Cu-10Ta; the breakdown follows the same general trend with time.

A process control agent (PCA), specifically, stearic acid, was utilized to investigate whether increased comminution could be achieved between Cu and Ta. Stearic acid, a long chain hydrocarbon, is typically used as a processing agent to prevent cold welding and to induce increased fracture during milling. It can be removed from the as-processed powder, by heating it under high vacuum to temperatures between 300 and 450° C. Once the stearic acid has been removed, the powder can then be used in any powder metallurgy based consolidation process for the production of bulk parts.

In Figure 10 the series of micrographs in the top and bottom rows, respectively, clearly reveal the positive effect of stearic acid as a function of time up to 6 hours. The use of stearic acid not only enhances the ability to increase the level of dispersion, but also improves the Ta particle refinement in Cu-10Ta. It is known that the increased dispersion is advantageous, as was revealed in the earlier smaller scale SPEX mill-based experiments demonstrating a critical link between the interrelationship of refined Cu grain and Ta particle sizes and a corresponding increase in mechanical performance. Therefore, the remaining milling trials for which powder production was scaled from 200 g to a kilogram size batch, relied on stearic acid as a PCA. It may be noted that the use of the PCA had another beneficial effect of increasing the powder quantity or yield, as it prevented cold welding of the Cu-Ta powder to the milling chamber and milling media.

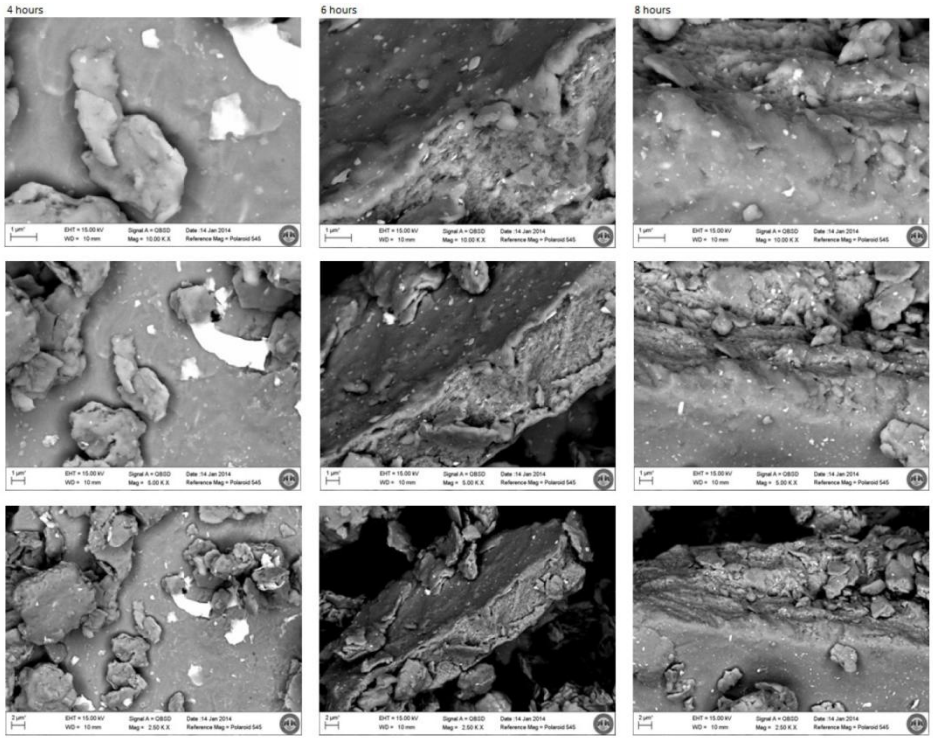

Figure 9: Backscatter electron mode scanning electron micrographs of Cu-1Ta as a function of milling time. Generally, distinct precursor grains of Ta are no longer evident as was in the case of Cu-10Ta and Cu-5Ta; the Ta breakdown follows the same general trend with time.

Data in Table 1 displays the results of the trace chemical analysis of the as-milled powders as a function of milling time for the Cu-Ta samples with 1, 5, and 10 at.% Ta. The data indicates that while other trace impurity elements are present within the milled powders, the primary contaminants picked up during milling appear to be Fe and Cr, which can directly be associated with the interactions between the milling media and chamber, both made of high-strength steel, and the Cu and Ta powders. Further, it can be seen that as a function of time, the level of Fe and Cr contamination scales with the Ta concentration. This is because, as the level of Ta increases, so does the hardness of the resultant Cu-Ta alloy. As such, the higher hardness causes increased wear by the grinding media and chamber which, in turn, leads to elevated levels of Fe and Cr being incorporated into the Cu-Ta powders during the milling process. To reduce this amount Fe and Cr, studies were performed in which the milling media and milling chamber were coated with pure Cu prior to milling. At this time, chemical analysis is still underway to quantify the benefit of pre-coating the media and chamber, but it is believed that processing in such a way should help to reduce the overall level of contaminants.

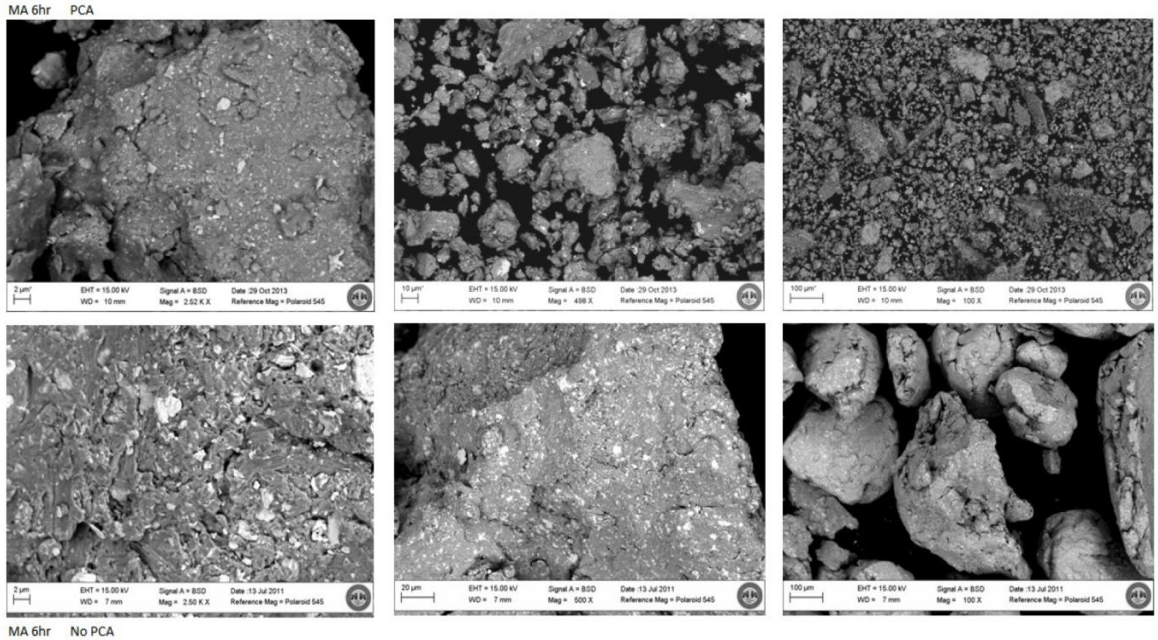

Figure 10: Backscatter electron mode scanning electron micrographs of Cu-10Ta as a function of milling time with and without stearic acid (note, this hydrocarbon is a typical process control agent used to prevent cold welding and increase the level of dispersion.) at increasing magnifications; top row: with stearic acid; and bottom row: without stearic acid.

Further analysis of interstitial impurity elements were performed on the as-milled powders. As shown in Table 2, of concern is the level oxygen pick up during the milling process. It is seen in the table that with increased time, greater levels of oxygen are incorporated into the Cu-Ta powders. With time this level increases and appears to saturate around 0.5 wt.% for both the

Cu-1Ta and Cu-10Ta powder compositions. Though, there is some inconsistency in the results, as much higher oxygen levels were detected for the Cu-5Ta powder composition. At this time, this is not well understood. Further experiments are currently being performed to assess whether oxygen could be removed or reduced during the milling or during the removal of the stearic acid PCA, where the as-milled powders could be heated under a pure hydrogen atmosphere at elevated temperatures.

X-ray diffraction analysis results as a function of milling time are shown in Figures 11 to 13 for the Cu-1Ta, Cu-5Ta, and Cu-10Ta powders, respectively. The full diffraction patterns from 10 to 90 or 30 to 100 degrees 2 Theta indicate that over the course of the milling process, the elemental Cu and Ta powders combine to form the various terminal Cu-Ta alloy compositions. In general, among the three data sets, it may be observed that, with increased milling time, for each of the fundamental Bragg reflections, the peak intensity decreases while peak width widens with the corresponding area under the peaks increasing as well. Additionally, the relative ratio of Ta to Cu peak intensity decreases. Both of these observations are consistent with alloying and simultaneous refinement of the Cu and Ta grain sizes. It is also noted that for higher Ta concentrations, there is a definite shift of the Ta peaks to lower scattering angles. The corresponding shift of the Cu peaks is not as noticeable. Regardless, this is an indication of mutual alloying between the elements. The extent of the shift is proportional to the amount of Cu incorporated into the Ta lattice or vice versa. Therefore, it is expected that at higher Ta concentrations this contraction will be greater. This is illustrated in the latter figures.

Table 1: Data shows the results of trace chemical analysis of the as-milled Cu-Ta powders as a function of milling time. The composition of the alloys tested were 1, 5, and 10 at.% Ta, respectively. The red box highlights the Fe results; the increasing levels arise from the milling chamber and grinding media.

Cu-10Ta	ELEMENT																
Time (MA)	P	S	Cr	Fe	Co	Cu	As	Ta	Si	Ge	Mg	Ni	Al	Mn	Total	Major	Minor
1	0.0154	0.0037	0.1114	0.4596	0.0804	77.6693	0.2857	21.3745							100.00	99.0438	0.9562
2	0.015	0.0035	0.1057	0.5106	0.1441	75.0072	0.2862	23.8507	0.0402	0.0369					100.00	98.8579	1.1422
4	0.0157	0.0053	0.1855	1.0416	0.2703	74.1021	0.2921	23.3815	0.1651	0.0462	0.448	0.0465			100.00	97.4836	2.5163
6	0.0161	0.0055	0.2962	2.2826	0.4073	71.9434	0.2691	22.9941	0.1956	0.0464	1.4799	0.0512	0.0125		100.00	94.9375	5.0624
8	0.0111	0.0108	0.3595	3.668	0.524	71.0028	0.2771	23.0297	0.1228	0.044	0.8716	0.0554	0.0233		100.00	94.0325	5.9676
10	0.0158	0.0107	0.3861	4.5092	0.6386	70.696	0.2704	22.7551	0.0786	0.0438	0.4688	0.069	0.0151	0.0428	100.00	93.4511	6.5489

Cu-5Ta	ELEMENT														TOTALS		
Time (MA)	P	S	Cr	Fe	Co	Cu	As	Ta	Si	Ti	Mg	Ni	Al	Cl	Total	Major	Minor
0	0.0181	0.009		0.0232		97.058	0.3916	1.8072	0.2525		0.4033		0.0297	0.0074	100.00	98.8652	1.1348
4	0.0159		0.0923	1.2398	0.1229	84.7829	0.334	13.4121							100.00	98.195	1.8049
6	0.0165	0.0068	0.152	2.4083	0.194	84.3742	0.3479	12.2836		0.1327		0.07	0.0139		99.98	96.6578	3.3421
8	0.0181		0.2101	3.5708	0.2779	83.3338	0.3339	12.0575	0.0275	0.0812		0.0894			100.00	95.3913	4.6089

Cu-1Ta	ELEMENT														TOTALS		
Time (MA)	P	S	Cr	Fe	Co	Cu	As	Ta	Si	Ti	Mg	Ni	Al	Cl	Total	Major	Minor
0															0.00	0	0
4	0.0173	0.0034	0.0917	0.8368	0.1086	95.2936	0.3661	3.2464							99.96	98.54	1.4239
6	0.0229	0.0045	0.1352	1.6459	0.1937	94.0737	0.382	3.4894	0.0202						99.94	97.5631	2.4044
8	0.0181	0.0056	0.1894	2.6537	0.27	93.1044	0.3693	3.3382	0.018						99.97	96.4426	3.5241

Large amount of Fe contamination observed as a function of milling time. More iron contamination present in samples with larger Ta content.

Weight Percent			
Cu	Ta		
75.97	24.03	10%	Atomic
86.97	13.03	5%	Percent
97.2	2.8	1%	Tantalum

Table 2: Oxygen impurity pick-up during the milling of the Cu-Ta powders with 1, 5, and 10 at.% Ta levels as a function of milling time.

	O2 (wt %)		
Milling Time	Cu-10Ta	Cu-5Ta	Cu-1Ta
0	0.05	0.05	0.05
1	0.71	-	-
2	0.68	-	-
4	0.71	1.06	0.85
6	0.64	0.76	0.53
8	0.56	2.48	0.46
10	0.46	-	-

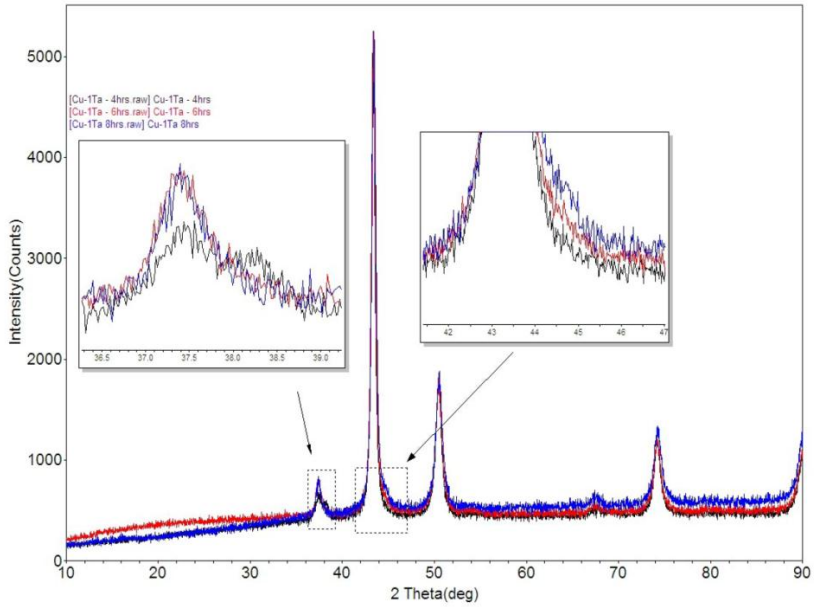

Figure 11: X-ray diffraction patterns as a function of milling time for the as-milled Cu-1 at.% Ta powder. All peaks show extensive broadening and well as a shift in both Cu and Ta peak positions. Additionally, observe the non-symmetrical shoulder broadening.

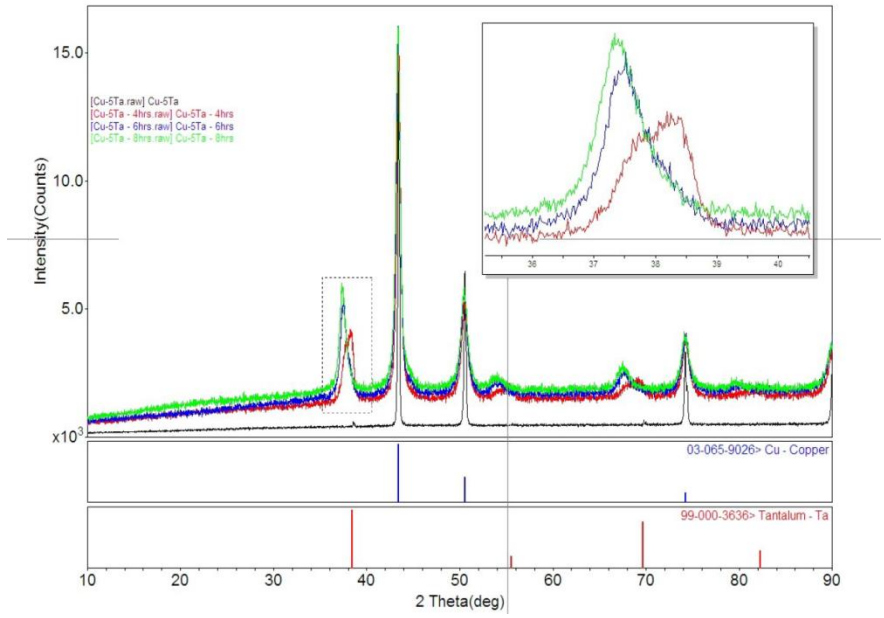

Figure 12: X-ray diffraction patterns as a function of milling time for the as-milled Cu-5 at.% Ta powder. The primary Ta peaks are observed to shift to lower scattering angles indicating alloy formation between Ta and Cu. All peaks show extensive broadening. Additionally, observe the non-symmetrical shoulder broadening.

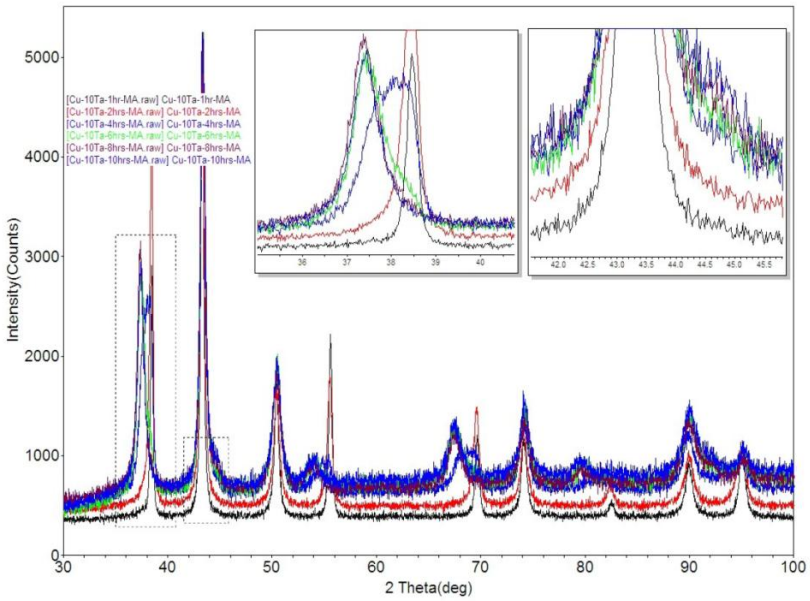

Figure 13: X-ray diffraction patterns as a function of milling time for the as-milled Cu-10 at.% Ta powders. The primary Ta peaks are observed to strongly shift to lower angles indicating significant alloy formation between Cu and Ta. Additionally, all peaks show extensive broadening.

The x-ray diffraction patterns were analyzed for the Cu and Ta grain sizes, respectively. Table 3 summarizes the results showing a decrease in both the Cu and Ta grain size. Both the average Cu and Ta grain size appears to be independent of the overall composition. That is, it is found to be the same or approximately the same average value, reached regardless of the composition. For Cu, the minimum grain size reached is approximately 17 nm, while for Ta, it is approximately 10 nm.

The as-milled powders were then consolidated into a series of small cylindrical rods, using hot isostatic pressing (HIPing) at various temperatures and pressures. Figure14 shows backscatter electron SEM images taken from polished cross-sections of these samples consolidated. In general, using an instrumented HIP unit with an in-situ eddy current sensor that measures densification rate, the technique was developed to identify the consolidation protocols which resulted in samples that were free from voids both at macroscopic and microscopic levels. Additionally, examination showed that prior particle boundaries were not observed, indicating that significant diffusion bonding was achieved between the individual particles, resulting in a fully dense well-bonded structure. It can be seen from the lower magnification images that with an increase in Ta concentration, there is a corresponding increase in the heterogeneity between Ta-poor and Ta-rich; that is, there are regions which are rich and void of Ta particles. Conversely, higher magnification images reveal that the smaller Ta particles remain approximately the same size regardless of overall Ta concentration. These Ta particles are proximately 100 to 200 nm in diameter and are heavily dispersed throughout the matrix.

Table 3: Reduction of Cu grain size and Ta particle size as a function of milling time. The respective grain and particles size values agree well with those observed in the earlier small scale studies.

Xtal Size	Cu-1Ta			
(nm)	4	6	8	6
Cu Primary	18.2	17.7	16.5	16.6
Ta Primary	6.7	12.6	15.1	13.3

Xtal Size	Cu-5Ta			
(nm)	0	4	6	8
Cu Primary	79.1	18.6	17.9	16.7
Ta Primary	55.5	7.9	9.1	9.8

Xtal Size	Cu-10Ta					
(nm)	1	2	4	6	8	10
Cu Primary	31.3	20.7	15.8	15.7	16.8	17.2
Ta Primary	40.9	27.9	7.8	8.9	11.9	11.6

Small rods machined out of the as-consolidated specimens were subjected to impact loading. As a function of composition, backscattered electron SEM images of the resultant fracture surfaces reveal ductile failure of the Cu-Ta alloy materials. It may be noted that at increasingly higher magnification levels, the images reveal similar topographies. Each of the samples has some indication of ductile failure behavior, exemplified by the dimpling observed within the fracture surface. Generally, on closer inspection of the high magnification images, small Ta particles are observed to be located within the centers of dimples. This fact is key to the fact that it is the Ta particles which are the likely initiation point of micro-voids, which then coalesce resulting in a catastrophic failure of the sample. Further, as can be seen in the high magnification images, the size of the corresponding dimples decreases with increased Ta concentration. This shows that a higher concentration of Ta particles will likely result in lower tension ductility.

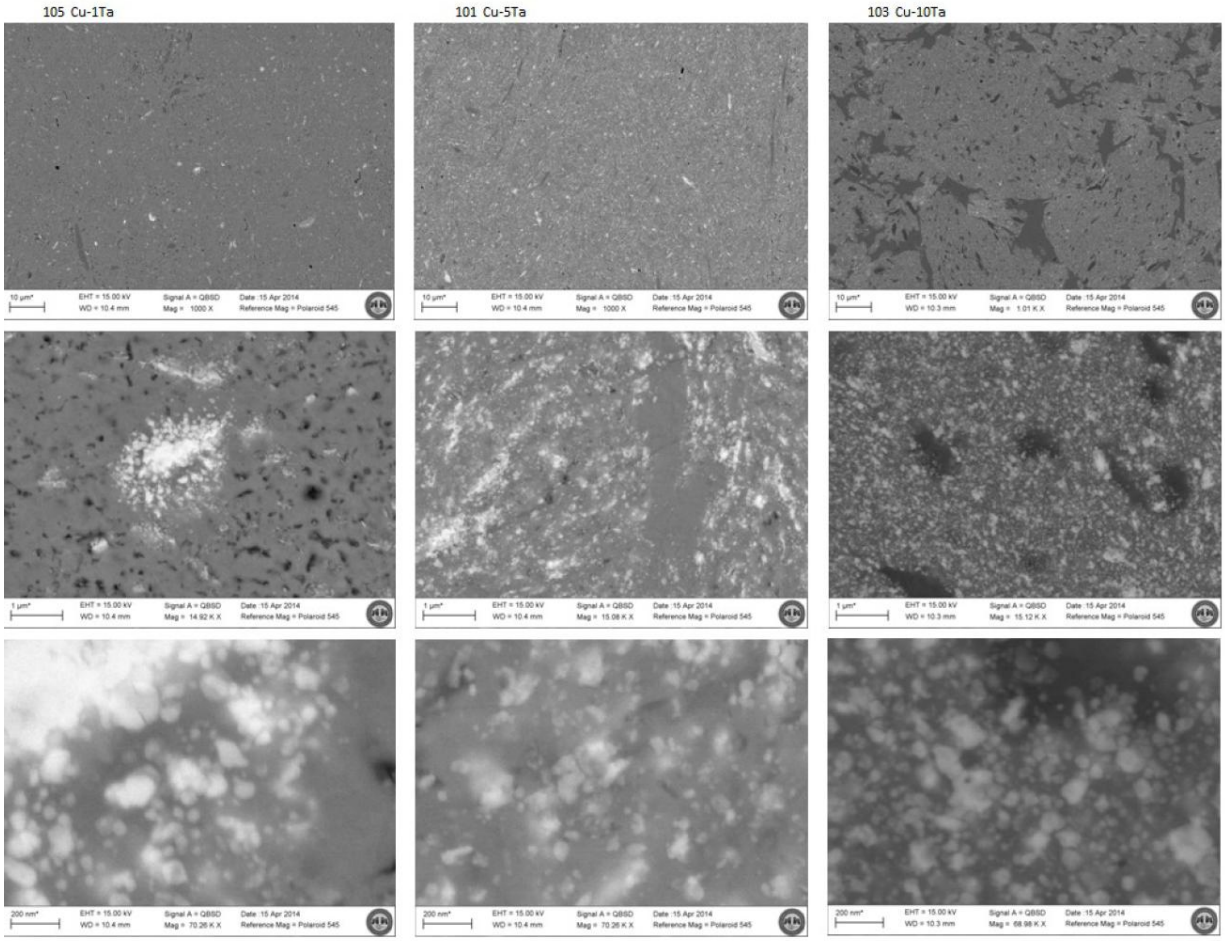

Figure 14: Backscatter electron mode scanning electron micrographs of the HIP consolidated Cu-Ta samples as a function of Ta concentration; 1, 5, and 10 at.% Ta. In the images, the dark gray areas correspond to Cu; and the light gray areas correspond to Ta. Once consolidated, increasing the Ta content results in a higher density of Ta particles. The images did not reveal the presence of porosity.

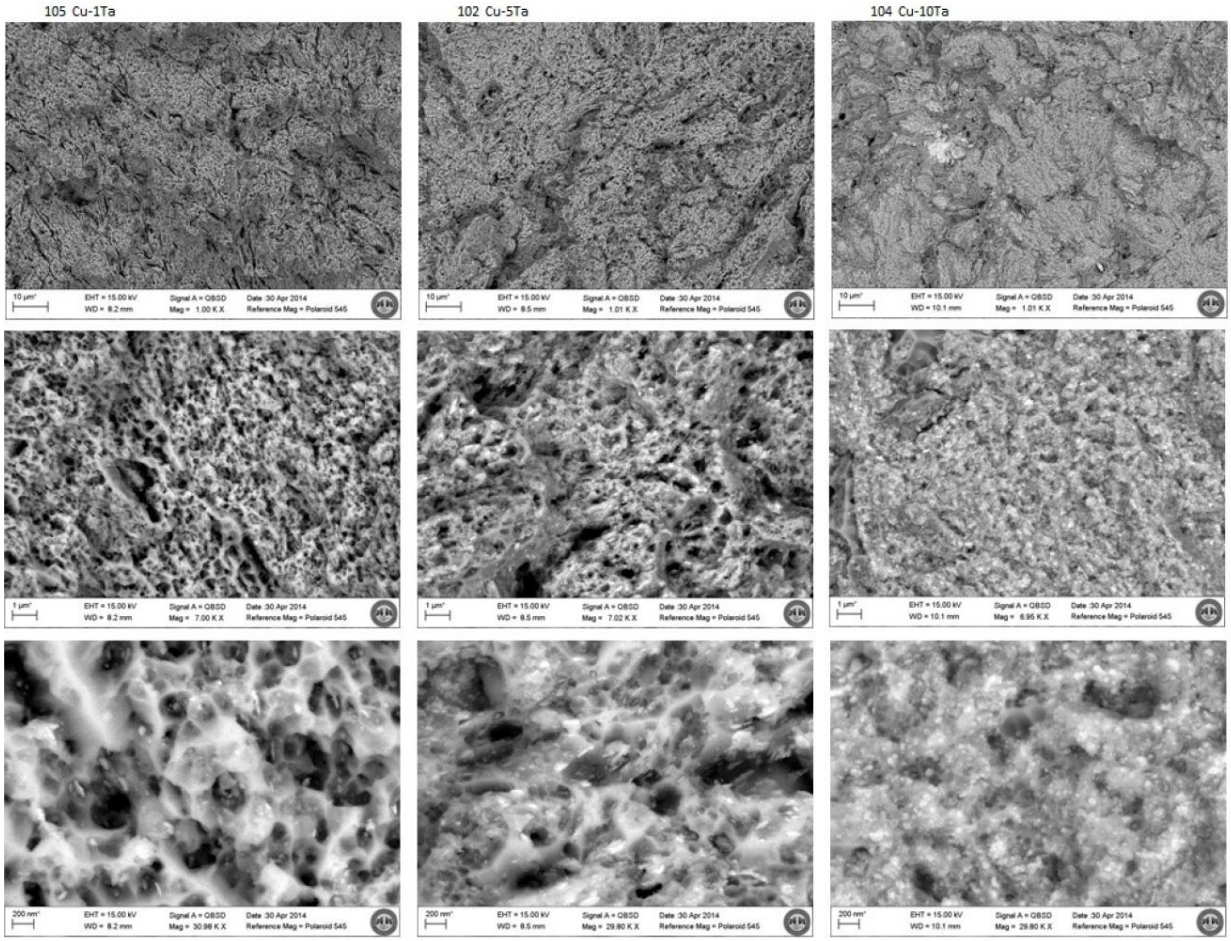

Figure 15: Backscatter electron mode scanning electron micrographs of fracture surfaces from the HIP consolidated Cu-Ta samples as a function of Ta concentration; 1, 5, and 10 at.% Ta. In the images, the dark gray areas correspond to Cu; and the light gray areas correspond to Ta. Note, larger Ta particles appear to be the nucleation sites for the formation of microvoids.

In addition to the examination of the as-milled powders produced using the large-scale milling facilities and the small bulk consolidates from subsequent HIP runs, in anticipation of the intended application, we also studied the tensile deformation behavior of the Cu-Ta alloys. Figure 16 reveals the tension ductility for an ECAE processed Cu-10Ta alloy, consolidated at various processing temperatures. It can be seen that for the Cu-10Ta alloy, the decrease in consolidation temperature results in an increase in yield and UTS strength, but at the expense of losing ductility. This is attributed to the onset and continued grain growth at the higher processing temperatures. In the figure, data for the Cu-1Ta sample is also included. It is interesting to note that just how much the strength increase with a relatively small change of Ta concentration.

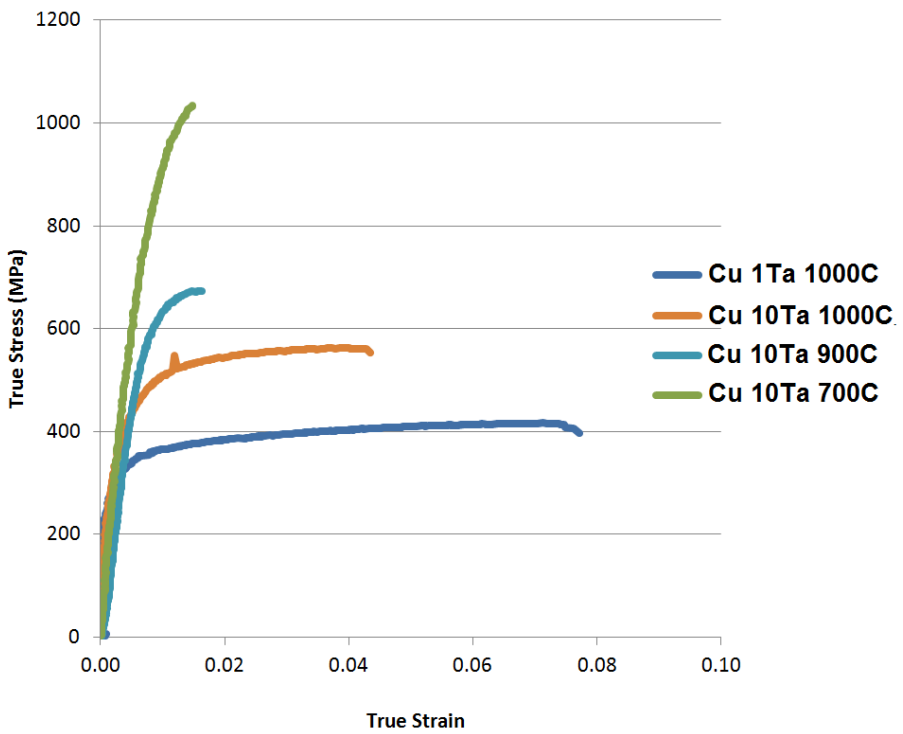

Figure 16: Tension ductility of the ECAE consolidated Cu-1Ta and Cu-10Ta samples, processed at various temperatures. Note the rapid drop in strenght and commensurate increase in ductility of the samples.

After the preliminary and fundamental characterization of the HIP consolidated parts, milling and powder production will was scaled up to kilogram quantities, specifically, for Cu containing 1 and 10 at.% Ta. Whereas smaller quantities of milled powders could be easily treated, these powders were degassed under vacuum at temperature of 450° C for 72 hours to remove the stearic acid PCA. After the powders were cleaned, they were loaded into specially designed HIP cans which enabled the production of near net shaped parts. Powder consolidation was performed at MATSYS Inc., located in Sterling, VA. This larger-scale process also relied on the use of an instrumented HIP, equipped with a larger eddy current sensor unit which allowed direct measurement of the diameter of the part or densification during sintering operations. The resultant parts shown in Figure 17, were produced at temperatures as high as 1000° C. The conical and hemispherical parts shown in the figure are in the as-HIPed condition. Note that this method is capable of producing a high surface quality as well as high dimensional accuracy. Also, these parts can be readily machined, as is illustrated by the outside surface of the hemispherical dome, to increase surface or dimensional accuracy.

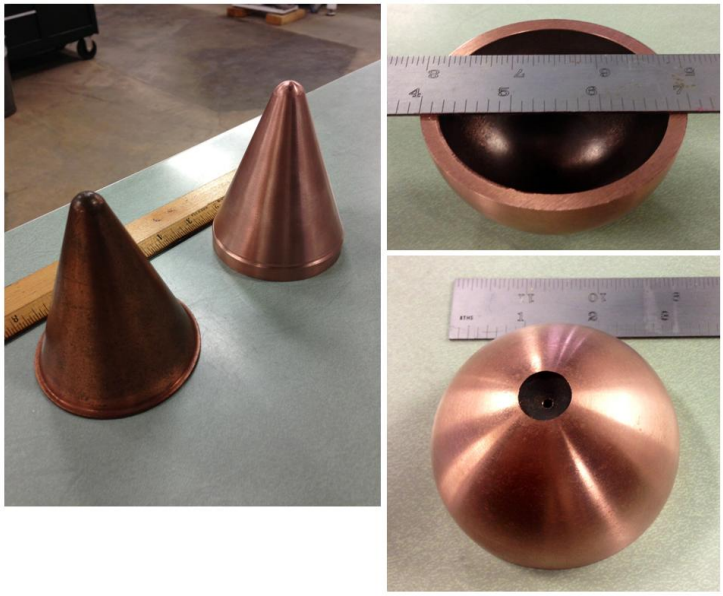

Figure 17: Macrophotographs of Cu-Ta alloy parts. The displays show near-net shaped conical and hemispherical geometries produced by instrumented HIPing of Cu-1Ta (cones) and Cu-10Ta (hemisphere). Note that the exterior surface of the hemispherical dome has been machined.

10. Conclusions:

A series of characterization techniques were utilized to study and develop a new family of nanocrystalline alloys based on the immiscible Cu-Ta binary system. Small and large-scale mechanical alloying was used to identify, assess, and map out how the physical and mechanical properties of this material scale from a proof-of-concept stage into a higher manufacturing environment. Experiments were conducted by tuning the composition from 1 to 10 at.% Ta. Microstructural evaluation and mechanical testing of the resultant alloys revealed that a diverse array of physical properties can be attained, which are intimately linked to the as-milled Cu grain size and the distribution of Ta particle dispersiods, both of which can be altered by altering the composition and consolidation methodology.

In combination the prior SERDP report and this current report reveal that Cu-Ta alloys are highly capable of meeting and exceed many of the properties exhibited by Cu-Be alloys. However, there still further research to be done to improve, optimize, and elucidate the existing alloy formulations towards a tangible application. The successful development of the instrumented HIP processing protocols demonstrates that parts fabrication is possible. Transitioning from small-scale processing in a SPEX mill (few grams/day) to larger scale processing (Zoz mill kilograms/day) reveals the need for a more critically designed process engineering study. It is expected that with such an additional effort, the level and role of impurities such as Fe, Cr, and oxygen on properties can be mitigated or greatly reduced. Additionally, evaluation of the physical and mechanical properties attained within the larger

scale dimensioned parts must be correlated to the properties achieved using smaller scale powder production equipment.

11. References:

1. M.E. Kolanz, Appl. Occup. Env. Hygiene, 16 (2001) 559-567.
2. Committee on Beryllium Alloy Exposures, Committee on Toxicology, National Research Council. Washington DC: The National Academies Press, 2008.
3. G.A. Day, et al., International Archives of Occupational and Environmental Health, 79 (2006) 161-164.
4. CNN, "Nearly 2,000 People Warned of Possible Beryllium Exposure," 2009. http://www.cnn.com/2009/HEALTH/01/29/los.alamos.beryllium/index.html accessed Jan. 31, 2010.
5. E.A. Brandes, *Smithells Metals Reference Book*. 6th ed., Butterworths London, 1983.
6. Brush Wellman "**Guide To Beryllium Copper,"** p.65.
7. M.A. Meyers, A. Mishra, and D.J. Benson, Prog. Mater. Sci., 51 (2006) 427-556.
8. K.S. Kumar, H. VanSwygenhoven, and S. Suresh, Acta Mater., 51 (2003) 5743-5774.
9. J.R. Weertman, in: C.C. Koch (Ed.) Nanostructured Materials: Processing, Properties, and Applications, Williams Andrews Publishing, New York, (2002) 397-421.
10. J.R. Weertman, D. Farkas, H. Kung, M. Mayo, R. Mitra, and H. Swygenhoven, MRS Bulletin, 24 (1999) 44-50.
11. C.C. Koch, Scripta Mater., 49 (2003) 657-662.
12. E. Ma, Scripta Mater., 49 (2003) 663-668.
13. Y.T. Zhu and X. Liao, Nature Mater., 3 (2004) 343-414.
14. K.M. Youssef, R.O. Scattergood, K.L. Murty, J.A. Horton, and C.C. Koch, Appl. Phys. Lett., 87 (2005) 091904-091904-091903
15. K.M. Youssef, R.O. Scattergood, K.L. Murty, and C.C. Koch, Scripta Mater., 54 (2006) 251-256.
16. Y.H. Zhao, X.Z. Liao, S. Cheng, E. Ma, and Y.T. Zhu, Adv. Mater., 18 (2006) 2280-2283.
17. F.J. Humphreys and M. Hatherly, Recrystallization and Related Annealing Phenomena, 2nd ed., Elsevier, Amsterdam, 2004.
18. L.C. Chen and F. Spaepen, J. Appl. Phys., 69 (1991) 679-688.
19. H. Gleiter, Prog. Mater Sci., 33 (1989) 223-315.
20. R. Birringer, Mater. Sci. Eng., A, 117 (1989) 33-43.
21. B. Gunther, A. Kumpmann, and H.-D. Kunze, Scripta Mater., 27 (1992) 833-838.
22. C.E. Krill, H. Ehrhardt, and R. Birringer, Z. Metallkd., 96 (2005) 1134-1141.
23. T. Frolov, K.A. Darling, L.J. Kecskes and Y. Mishin, Acta Mater. 60 (2012) 2158-2167.
24. W.H., R., Journal of the American Ceramic Society, 64 (1981) 19-22.
25. R.A. Andrievski, Int. J. Powder Metall. 30 (1986) 59-66.
26. J.D. Hansen, et al., J. Amer. Ceram. Soc., 75 (1992) 1129-1135.
27. J.R. Groza and R.J. Dowding, Nanostruct. Mater., **7** (1996) 749-768.
28. S.N. Mathaudhu, K.T. Hartwig and I. Karaman, J. Non-Crys. Solids, 353 (2007) 185.
29. J. Li, T. Malis and S. Dionne, Mater. Character., 57 (2006) 64.

12. Appendix:

Acta Materialia publication entitled "Microstructure and Mechanical Properties of Bulk Nanostructured Cu-Ta Alloys Consolidated by Equal Channel Angular Extrusion," by Darling, KA, Tschopp, MA, Guduru, RK, Yin, WH, Wei, Q, and Kecskes, LJ, Acta Materialia, 76, 168-185, September 2014.

Available online at www.sciencedirect.com

ScienceDirect

Acta Materialia 76 (2014) 168 185

Acta MATERIALIA

www.elsevier.com/locate/actamat

Microstructure and mechanical properties of bulk nanostructured Cu–Ta alloys consolidated by equal channel angular extrusion

K.A. Darling [a,*], M.A. Tschopp [a], R.K. Guduru [b], W.H. Yin [c], Q. Wei [c], L.J. Kecskes [a]

[a] *US Army Research Laboratory, Weapons and Materials Research Directorate, Aberdeen Proving Ground, MD 21005, USA*
[b] *Department of Mechanical Engineering, University of Michigan, Dearborn, MI 48128, USA*
[c] *Department of Mechanical Engineering and Engineering Science, University of North Carolina at Charlotte, Charlotte, NC 28223, USA*

Received 21 March 2014; received in revised form 25 April 2014; accepted 30 April 2014
Available online 9 June 2014

Abstract

Nanostructured Cu–Ta alloys have shown promise as high-strength nanocrystalline materials in part due to their limited grain growth at high temperatures. In the present study, Cu–Ta alloy powders, synthesized via high-energy cryogenic mechanical alloying, were consolidated into bulk nanostructured specimens using equal channel angular extrusion (ECAE) at high temperatures. Subsequent microstructure characterization indicated full consolidation, which resulted in an equiaxed grain structure for the Cu matrix along with the formation of fine Ta precipitates, the size distributions of which varied both with composition and processing temperature. Microhardness, compression and shear punch testing indicated, in some cases, an almost threefold increase in mechanical properties above that predicted by Hall–Petch estimates for pure nanocrystalline Cu. Stress relaxation tests substantiated the strain-hardening behavior and grain-size-dependent dislocation activity observed in the nanocrystalline Cu–Ta samples.
Published by Elsevier Ltd. on behalf of Acta Materialia Inc.

Keywords: Nanocrystalline alloys; Cu Ta alloys; Equal channel angular pressing; Mechanical behavior; Dynamic compression test

1. Introduction

Nanocrystalline and nanostructured materials have spawned significant interest due to the unique set of properties unachievable by coarse-grained polycrystalline materials. However, synthesis and consolidation of these nanostructured materials into bulk parts is often very challenging, attributed in part to limitations in processing methods that are not easily scalable (e.g. electrodeposition, vapor deposition) or due to uncontrolled grain growth of the non-equilibrium structure during processing. The synthesis of novel nanostructured alloys formed from forced solid solutions between elemental Cu and immiscible solute species has been the focus of several recent studies [1–7]. These non-equilibrium solid solutions have been shown to evolve and form well-dispersed nanoscale composite alloys upon annealing at elevated temperatures. In some cases, the coarsening mechanism observed after phase separation in such alloys has been attributed to the segregation and diffusion of the immiscible solute species along grain boundaries [2,5]. While both simulations and experiments indicate remarkable physical properties for this new class of materials [1,5,8,9], to date only small-scale testing methods (e.g. microhardness measurements) have been used to probe the deformation mechanisms due to limitations in producing bulk test specimens. It is well known that there are often size effects in mechanical properties (e.g. micropillar compression [10]), hence further work with bulk consolidated nanostructured Cu alloys can help to accurately assess the representative mechanical properties and behavior of bulk parts.

* Corresponding author.
E-mail address: kristopher.darling.civ@mail.mil (K.A. Darling).

http://dx.doi.org/10.1016/j.actamat.2014.04.074
1359-6454/Published by Elsevier Ltd. on behalf of Acta Materialia Inc.

There are several processing methods that can be used to readily produce nanocrystalline microstructures consisting of solid solutions of different elements. For instance, severe plastic deformation has been successfully used over the last couple of decades to generate non-equilibrium microstructures in metals [11–13]. Concurrently, high-energy mechanical alloying has been used successfully, and has become an established processing method for studying nanocrystalline and non-equilibrium solid solutions [11,14,15]. Recently, mechanical alloying has been used to generate Cu-based powders composed of immiscible alloying elements such as Ta [5,9], W [16], Zr [17] and Nb [18]. These systems have shown moderate to extraordinarily high microstructural stability at elevated temperatures. Despite the lack of consensus on the exact mechanism of stability, be it through thermodynamic mechanisms (grain boundary (GB) energy reduction) or kinetic mechanisms (the dispersion of second-phase nanoscale particles, which work as Zener pinning centers of the GBs), these microstructures allow for bulk nanocrystalline samples to be generated and tested.

There have been a number of recent findings on the thermal stability and microstructure of a high-strength nanocrystalline Cu–Ta alloy. For instance, isothermal annealing of a Cu–10% Ta alloy[1] produced via high-energy cryogenic mechanical alloying resulted in a nanocrystalline, two-phase composite structure of spheroidal Ta particles and nanolamellar Ta structures dispersed in a Cu-rich Cu–2% Ta alloyed matrix [5]. Grain size analysis by X-ray diffraction estimated the size of the Cu–Ta solid solution grains and dispersed Ta phases to be 6.7 and 6.0 nm, respectively. However, larger Ta particles were also observed during transmission and scanning electron microscopy (TEM and SEM) imaging of samples prepared from as-milled powder particles. During high-temperature annealing, it was also reported that the Cu–Ta alloys undergo phase separation of the as-milled forced solid solution and grain growth of the resultant nucleating phases. Recent atom probe results (not presented here) indicate that a significant volume fraction of Ta atomic clusters result from this decomposition process. After continued heating to high temperatures (>600 °C), the microstructure coarsens and evolves to a state composed of nanocrystalline Cu-rich grains and uniformly dispersed Ta particles. The dispersion contains particles as small as atomic clusters [5] or particles hundreds of nanometers in diameter, with their individual volume fractions being dependent on the final anneal temperature reached. Ultimately, the Cu grain structure is sufficiently stabilized at high temperatures by particle pinning effects, wherein the retention of nano- or ultrafine grains at very high homologous temperatures (97% T_m) is allowed [5].

The evolution of the coarsening process should be directly related to the overall content of Ta in the Cu–Ta alloy, with a lower thermal stability observed for lower Ta concentrations. That is, it is hypothesized that the Cu grain size stability, the Ta particle size distribution and the associated mechanical properties are expected to be different for Cu alloys with lower Ta concentrations (e.g. 1% Ta used herein) as compared to those with higher amounts of Ta (e.g. 10% Ta) at any given temperature. In the present work, this hypothesized difference in microstructure, thermal stability and mechanical properties of lower Ta concentrations in Cu–Ta alloys is shown to be the case.

While the high-temperature stability of Cu–Ta alloys may inhibit their ability to be sintered under conventional powder processing conditions, the improved thermal stability over nanocrystalline Cu opens alternative processing regimes. This, in turn, can allow for full densification and, hence, the retention of the unique nanocrystalline structures using alternative consolidation approaches. In particular, the combination of pressure and shear at elevated temperatures, as in hot equal channel angular extrusion (ECAE), could result in full densification of these materials. Specifically, the ECAE process subjects a billet to a pure state of shear as material flows around an L-shaped channel [19–23]. Moreover, ECAE can be performed at elevated temperatures for any number of passes and the billet can be rotated between passes to provide precise texture control for the material [19–23]. This mode of severe plastic deformation has previously been very effective in consolidating powders that have a very narrow processing window and cannot be easily consolidated using conventional methods, such as high-hardness, brittle metallic glass powders [24–26]. Using this laboratory-scale technique, bulk specimens consolidated from powders have been generated in sizes that are suitable for small-scale mechanical testing experiments (on the order of 0.5 cm).

Small-scale testing techniques are an effective way of evaluating novel and scarce materials, as the quantity of available material often precludes the use of conventional testing dimensions and geometries which require much larger material volumes. Shear punch testing has recently been gaining attention as one such technique [27–29]. In addition to minimal sample preparation, the spatial resolution is quite high, so only 1–2 mm^2 of surface area is required for an individual test. In the past few years, this technique has been employed to ascertain deformation mechanisms and characterize material properties of nanocrystalline materials by (i) utilizing various tests, such as stress relaxation tests, and (ii) determining the underlying material properties, such as the activation volume associated with plastic deformation [29,30]. The physical activation volume is critical for determining the rate-controlling step of the specific plastic deformation mechanism that governs the plastic deformation processes of nanocrystalline metals; it is related to the strain-rate sensitivity of the material, and it has a definite value and stress dependence for each atomic process [31–33].

The research objective of the present study is to understand the microstructure, thermal stability and mechanical

[1] Atomic per cent of Ta is used as a convention throughout the present work.

behavior of bulk-consolidated nanocrystalline Cu–1% Ta and Cu–10% Ta alloys. The Cu–Ta alloyed powders used herein were consolidated using high-temperature ECAE to form bulk nanostructured composite materials. The powders were consolidated and processed in such a way as to create different grain sizes, ranging from 60 to >200 nm, with different particle size distributions of the dispersed Ta as well. The samples were prepared and tested utilizing a small-scale shear punch test (SPT) method for quasi-static loading and the Kolsky bar testing (or Split–Hopkinson pressure bar) technique for high strain rate loading. The reasons for performing high strain rate loading experiments are twofold. First, to our knowledge, little is known about the high strain rate or dynamic mechanical properties of ultrafine-grained and nanocrystalline metals, particularly for those with a face-centered cubic structure [34–37], including Cu. Second, the high strain rate response of structural materials is of great importance in many areas, including high-speed machining, and automotive and defense applications. It has been established that ultrafine-grained and nanocrystalline metals with body-centered cubic structures exhibit a unique and extraordinary behavior under high strain rate loading, such as adiabatic shear localization, primarily attributed to a highly elevated strength, diminished strain-hardening capacity and reduced strain-rate sensitivity [31,38]. Therefore, it is important to ascertain whether such behavior will also be exhibited by an extremely strong nanocrystalline Cu.

The primary interest of the present work, however, is the mechanical response of Cu–Ta alloys, analyzed to obtain the activation volume and identifying the dominant strengthening and plastic deformation mechanisms. Additionally, the effects of grain-size reduction, particle size and particle distribution (from atomic clusters to larger incoherent precipitates) on the mechanical response were of interest. In the context of the ECAE processing method applied, these results and the evolution of the microstructure are described.

2. Experimental procedures

2.1. Cu–Ta alloy powder processing

High-energy cryogenic mechanical alloying was used to synthesize Cu–1% Ta and Cu–10% Ta powders. For each of the compositions, appropriate amounts of Cu and Ta powders (−325 mesh, 99.9% purity) with a total weight of 5 g were loaded into hardened steel vials along with the milling media (440C stainless steel balls) with a ball-to-powder ratio of 10-to-1 by weight, and then sealed inside a glove box in Ar atmosphere (oxygen and moisture are <1 ppm). Ball milling was carried out in a SPEX 8000 M shaker mill at cryogenic temperatures (verified to be ~−196 °C) using liquid nitrogen. This was accomplished by placing the steel vial in a thick polymer sleeve that was fixed in the high-energy mill with a provision for liquid nitrogen flow around the vial via inflow and outflow vents. The vial was equilibrated for 20 min to reach a temperature of around −196 °C before the milling was started. All of the Cu–Ta powders were milled for 8 h. After completion of the milling cycle, the vials were opened inside the glove box and the powders were stored therein. This process was repeated until a total powder charge of 100 g for each composition was attained. Cryogenic mechanical milling resulted in an unagglomerated powder mass with a particulate size range of 20–100 μm. Copper sheet stock (99% purity) was used as a baseline coarse-grained material for comparison.

2.2. Bulk powder consolidation via ECAE

For the ECAE consolidation experiments, the as-milled powders were placed into nickel cans and sealed inside the glove box. The nickel cans were created by taking billets of nickel 201 alloy having dimensions of 25.4 mm × 25.4 mm × 90 mm and drilling an ~10 mm diameter hole (~50 mm length) along the long axis of the billet. This created a powder chamber for emplacing the as-milled Cu–Ta powders which was later sealed shut. Prior to ECAE, the die assembly was heated to 350 °C. The nickel cans loaded with as-milled powders were equilibrated (for 40 min) in a box furnace purged with pure Ar gas at 700 and 900 °C, respectively. The equilibrated cans were then quickly removed from the furnace, dropped into the ECAE tooling and extruded at an extrusion rate of 25.5 mm s^{-1}. This procedure was repeated four times following route B_c [19–23]. The ECAE tooling had a channel angle of 90°. The four consecutive extrusions resulted in a total strain of ~450%. Some of the extruded cans were then either serial sectioned for shear punch testing or cut into compression samples using wire electric discharge machining. Through SEM imaging of the exposed surfaces, the extracted specimens were found to be fully consolidated samples with no evidence of prior particle boundaries or visible porosity.

2.3. Pre-testing sample preparation

For shear punch and compression specimens, the following technique was used to prepare the relevant surfaces. The as-consolidated samples were thinned down to approximately 300 μm and polished on both sides to a mirror finish. This was accomplished by successive polishing using a standard metallurgical preparation methodology of grinding with 300, 600, 1000, 2400 and 4000 grit SiC paper, followed with fine polishing using alumina pastes composed of 1 or 0.5 μm particles suspended in water. This preparation sequence was done prior to all mechanical tests to avoid the influence of any surface scratches on the measured mechanical properties.

2.4. Microstructural characterization

Microstructural analysis was performed with TEM using a JEOL JEM 2100 LaB_6 transmission electron

microscope operated at 200 kV. The TEM samples were prepared by slicing several wafers from the ECAE-processed compacts. A Gatan 659 disk punch was then used to cut 3-mm-diameter disks from the thin wafer. Subsequently, the disk was mounted on Gatan 623 disk grinder to further thin the sample to ~50 μm. Lastly, the specimen was transferred to a Gatan 656 dimple grinder to further thin the middle section. The final thickness of the middle section of the specimen was required to be less than 5 μm. Finally, a Gatan 691 precision ion polishing system was used to obtain electron transparency in the middle part of the specimen.

The grain size distributions of both the Cu matrix and the Ta particles or precipitates were calculated by counting a statistically significant number of grains. In cases where the distribution was found to be bimodal, a particle size of 30 nm was chosen as the demarcation point to separate the two modes.

2.5. Mechanical property measurements

Standard Vickers microhardness measurements were performed on a Wilson Hardness Tukon 1202 equipped with a 1000X lens system and performed under ambient conditions with a load of 50 gf and a loading time of 10 s. The quasi-static compression experiments were performed on an MTS 810 hydro-servo loading system (with a self-alignment feature) at a strain rate of $8 \times 10^{-4}\,s^{-1}$. The dimensions of the cuboid-shaped samples for quasi-static compression were approximately 5.0 mm × 2.5 mm × 2.5 mm. The loading and side faces of the specimens were well polished before performing the experiments (Section 2.4). The interface between the loading faces and the tungsten carbide platens was carefully lubricated to mitigate any friction effects. The strain rate of quasi-static compression was controlled by the cross-head speed of the loading system. Dynamic high strain rate ($\sim 10^3\,s^{-1}$) compression tests were performed using a standard Kolsky bar system operated under ambient conditions. In this experiment, a stress wave is generated in an elastic input bar by the impact of a striker bar launched from a gun barrel by pressurized gas released from a gas tank. The stress wave travels down the input bar and loads the specimens, which are sandwiched between the input and output bars. Part of the stress wave is reflected into the input bar and part of it is transmitted into the output bar. The coaxial striker and the input and output bars consist of high-strength maraging steel, all having the same diameter. Strain gauges are attached to the input and output bars, and the wave signals are recorded by an ultrahigh-speed multi-channel oscilloscope. Processing of the reflected and transmitted wave signals results in the high strain rate ($\sim 10^3\,s^{-1}$) stress–strain curves of the specimen. The post-loaded specimens may be recovered for examination to obtain information regarding ongoing dynamic plastic deformation or failure mechanisms. The principles, precautions and caveats for using this technique can be found in the recent monograph by Song and Chen [39], or in standard handbook articles [40,41].

Shear punch testing is a small-scale specimen testing technique; the primary advantage of the technique is the small volume of sample that is required for testing. Fig. 1 shows the SPT apparatus used in the current characterization effort. An Instron 1123 load frame equipped with a 5 kN load cell was used to perform a standard shear punch test, as well as three different types of relaxation test (Single, Type I and Type II). Fig. 1 shows the three stress relaxation test types utilized in the present work. The Single relaxation test simply ramps to an initial load, then measures the relaxation of that load with time. The Type I relaxation test successively ramps the stress to levels above the yield strength at a particular time interval and measures the relaxation of that stress with time (all within the same test), with the later stress being higher than the earlier stress between two consecutive ramps. The Type II relaxation test successively ramps to the same stress level (above the yield strength) at a particular time interval and measures the relaxation of that stress with time (all within the same test). In this manner, the Type I and Type II relaxation tests measure the relaxation response associated with microstructure evolution (and, in some instances, strain hardening) from prior relaxation cycles. While the shear stress can be calculated from the load, the complex strain state prevents a true measure of strain; thus, while this is not a "true" stress–strain curve, as with other techniques, valuable information can still be gleaned from these experiments (e.g. yield shear stress, ultimate shear stress, activation volumes). For instance, the present experiments were used to obtain the apparent activation volume V_r, which is influenced by changes in the mobile dislocation density, and the physical activation volume, V^*, which is influenced by the constant mobile dislocation density values. The physical activation volume is a critical parameter for determining the specific deformation mechanisms governing ductility in nanocrystalline metals and is related to the strain-rate sensitivity of the microstructure through the following relationships [31,42]:

$$m = \frac{d \ln \tau}{d \ln \dot{\tau}} \tag{1}$$

$$V^* = \frac{kT}{m \cdot \tau} \tag{2}$$

Eq. (1) provides the formula for the derivation of the strain-rate sensitivity (m) based on stress relaxation experiments, where $\dot{\tau}$ is the rate of change of the shear stress during the stress relaxation. In Eq. (2) T and k are the temperature and the Boltzmann constant. Since measurement of the strain-rate sensitivity and the activation volume usually assumes a constant microstructure, only the data in the early stage of the stress relaxation can be used. Stress relaxation tests were performed on disk-shaped samples using the SPT apparatus. The measured activation volumes in both of the Cu–Ta alloys shed light on the operating plastic

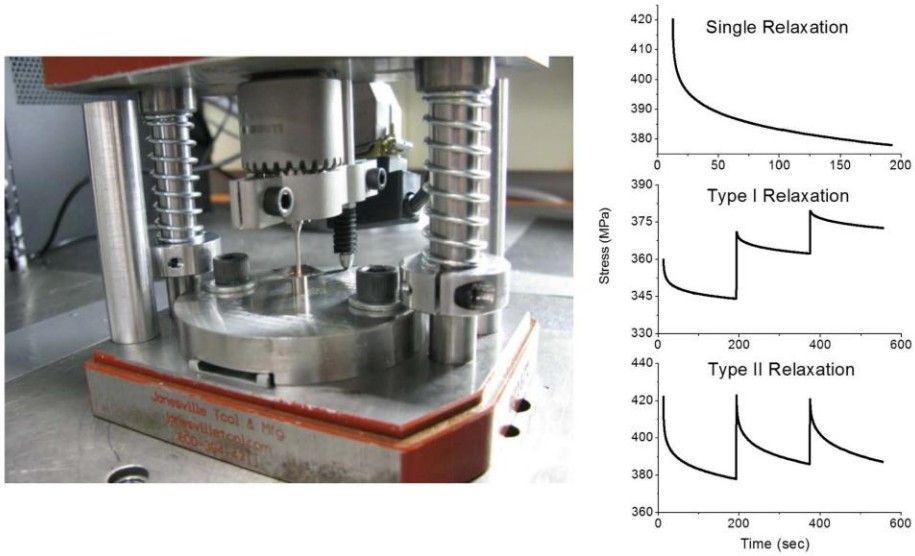

Fig. 1. The SPT apparatus, with the punch, specimen and tungsten carbide platen in place (left); and the three different types of stress relaxation tests (Single, Type I and Type II) utilized in the present experiments (right). Note the differences in the relaxation tests: stress is successively ramped in Type I relaxation tests, whereas the stress is maintained at a fixed level in Type II relaxation tests.

deformation mechanisms. More information on the SPT methodology and measurements can be found in the literature [29–32]. All the standard SPTs were done at room temperature using small disk-shaped samples with a diameter of 1.0 mm at a displacement rate of (0.01 in min^{-1}).

3. Results

3.1. Microstructure characterization

Typical microstructures for ECAE-processed Cu alloys containing 1 and 10% Ta, consolidated at different temperatures, are presented in Fig. 2. Specifically, the three different Cu–Ta samples analyzed were: (i) Cu–1% Ta sample, ECAE processed at 700 °C (Fig. 2a); (ii) Cu–10% Ta, ECAE processed at 900 °C (Fig. 2b); and (iii) Cu–10% Ta, ECAE processed at 700 °C (Fig. 2c). These alloy samples are heretofore referred to as Cu–1Ta-700 °C, Cu–10Ta-900 °C, and Cu–10Ta-700 °C, respectively. A fourth sample of pure, coarse-grained Cu (not shown in Fig. 2) with an average grain size of 10 μm (determined by optical microscopy) has been included for reference. The corresponding histograms for the Cu matrix grain size with the relevant statistics for all three Cu–Ta alloys are provided in Fig. 3.

The grain growth of the Cu matrix in all three Cu–Ta alloys is quite limited, despite the very high consolidation temperatures used during the ECAE process. The Cu matrix grains for all of the samples are equiaxed in nature. Further, as shown in Fig. 3, the Cu–10Ta-900 °C has a wider grain size distribution (up to 500 nm) than the other two Cu–Ta alloys, which were consolidated at the lower temperature of 700 °C. When comparing the microstructures of Cu–10Ta-900 °C and Cu–10Ta-700 °C to those reported earlier [5,9] that were heated to similar temperatures, the ECAE consolidated microstructures have undergone more coarsening due to process consolidation. For instance, the ECAE-processed Cu–10Ta-900 °C sample has a mean grain size of 213 nm, which is significantly larger than that reported for Cu–10% Ta annealed at 900 °C, or even at the 1040 °C discussed in Ref. [5]. The mean Cu matrix grain sizes of the ECAE-processed Cu–1Ta-700 °C and Cu–10Ta-700 °C samples are 168 and 70 nm, respectively.

Analysis of these and other micrographs indicates that precipitation of Ta occurs throughout the entire microstructure (Fig. 2a–c). The Ta precipitates are circled in the figure for identification relative to the Cu matrix grains. The precipitates are observed within the Cu matrix grains as well as at the grain boundaries for both Cu–10Ta-700 °C and Cu–10Ta-900 °C, irrespective of the consolidation temperature. However, the precipitation of Ta is not as clearly discernible in the Cu–1Ta-700 °C alloy (Fig. 2a). Fig. 4 provides the Ta particle size histograms for all three samples after ECAE processing. Additionally, Table 1 provides the collective statistics from Figs. 3 and 4, together with a summary of our significant findings for both the Cu matrix grain size and Ta particle size for the three samples. A bimodal particle size distribution exists for the two 10% Ta samples; therefore, for these samples

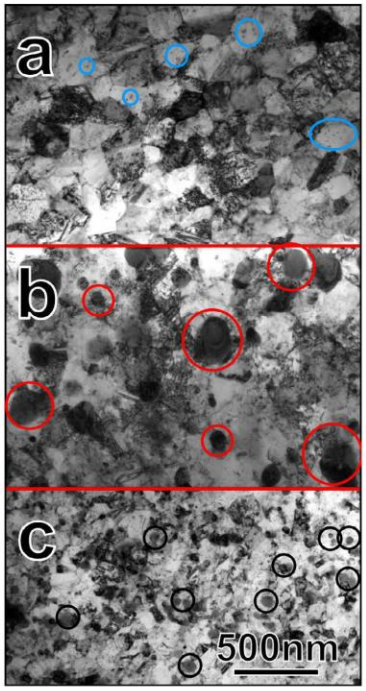

Fig. 2. TEM images of the Cu–Ta microstructures of the as-ECAE-consolidated composites: (a) Cu–1Ta-700 °C, (b) Cu–10Ta-900 °C and (c) Cu–10Ta-700 °C. Circles identify the Ta precipitates for the Cu–1Ta-700 °C (blue), Cu–10Ta-900 °C (red) and Cu–10Ta-700 °C (black) samples. Note the effect of Ta concentration and ECAE consolidation temperature the Ta precipitate size. (For interpretation of the references to colour in this figure legend, the reader is referred to the web version of this article.)

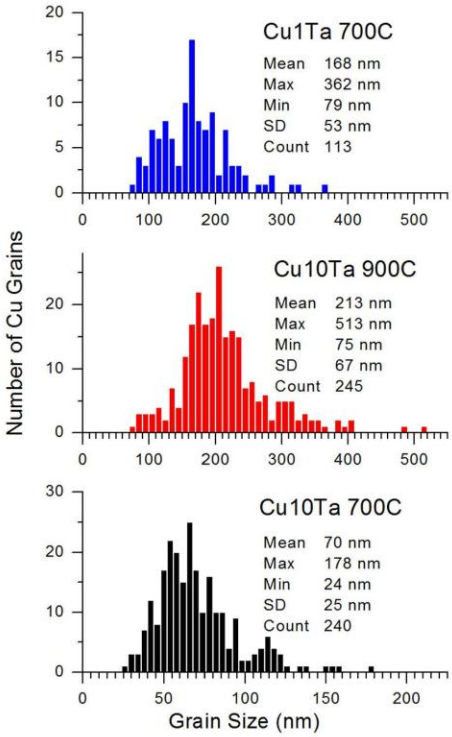

Fig. 3. Cu matrix grain size histograms for the Cu–Ta alloys: Cu–1Ta-700 °C (top), Cu–10Ta-900 °C (middle) and Cu–10Ta-700 °C (bottom). The grain size distributions of the first two alloys, Cu–1Ta-700 °C and Cu–10Ta-900 °C, are roughly similar, while the grain size distribution for the third, Cu–10Ta-700 °C, has shifted to a much finer grain size.

two sets of means are provided. With increasing consolidation temperature, the average of these distributions increases and the distribution becomes more spread out. It is interesting to note that for all three samples, Cu–1Ta-700 °C, Cu–10Ta-900 °C and Cu–10Ta-700 °C, there are a large number of fine particles with a diameter of approximately 10 nm. In the case of Cu–1Ta-700 °C, the distribution of Ta particles is almost entirely composed of these smaller Ta precipitates. That is, as the concentration of Ta is decreased from 10% to 1%, the distribution is restricted to only the smaller Ta precipitates. As such, it is expected that the coarsening kinetics of the Ta particles will be heavily reduced in the 1% Ta samples due to the lack of available Ta solute required for coarsening.

Fig. 5 provides higher resolution TEM bright-field images showing the bimodality of the Ta particle distribution in the Cu–10Ta-900 °C alloy. Interestingly, in both of the 10% Ta samples, the Ta particles that occupy GB positions (marked with red dots) are significantly larger than particles trapped in the Cu grain lattice (surrounded by red circles). This phenomenon can be explained by the ability of Ta atoms to diffuse along grain boundaries in contrast to the Cu lattice, where diffusion of the dispersed Ta atoms is extremely slow, even at temperatures near the T_m of Cu [9]. Hence, the resultant Ta particle distribution of the samples can range in size from a few nanometers to >100 nm. In addition to the TEM observations, the authors' recent unpublished atom probe investigations of Cu with 10% Ta confirm that a significant volume fraction of Ta atomic clusters resides within the Cu matrix. Such a wide size distribution lends itself to a complex range of hardening mechanisms operating to strengthen the matrix; this has been seen in the analogous γ' precipitate strengthening of Ni-based superalloys [43,44].

3.2. Mechanical properties

3.2.1. Indentation

Table 2 displays the mechanical property data (computed compression and shear yield strengths) obtained from indentation tests, which indicates that the microhardness of Cu–10Ta-700 °C is much higher than that of the

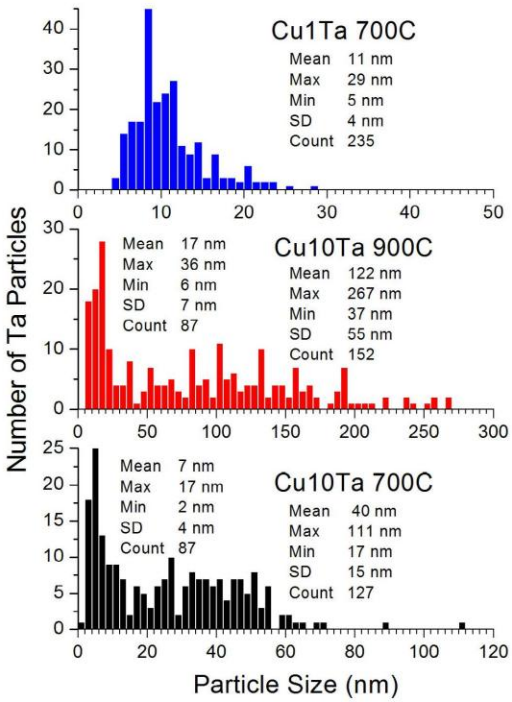

Fig. 4. Ta particle size histograms of the three Cu–Ta alloys: Cu–1Ta-700 °C (top), Cu–10Ta-900 °C (middle) and Cu–10Ta-700 °C (bottom). The latter two alloy samples have a bimodal Ta particle size distribution, so two sets of grain size statistics are provided for these two samples. The lower initial Ta concentration for Cu–1Ta-700 °C sample may contribute to the absence of the larger Ta particles.

other samples. In contrast, the microhardness of Cu–1Ta-700 °C is quite close to that of Cu–10Ta-900 °C (~2.1 GPa). This information complements the microstructure evaluation with respect to the Cu matrix grain size and the Ta particle size. The Cu–10Ta-900 °C sample has a larger mean grain size and wider grain size distribution, and it also has a much larger volume fraction of the Ta phase, be it in the form of clusters or Ta particles. This fact may compensate for any loss in GB strengthening when compared to the narrower grain size distribution of the Cu–1Ta-700 °C sample. However, in the end, both samples contain an appreciable amount of strengthening due to Ta, though probably from different mechanisms. Comparison of the hardness of these ECAE-processed Cu–Ta samples to pure nanocrystalline Cu of similar grain size, collected from literature data, indicates a strength increase by greater than a factor of two (~1 GPa for pure Cu vs. ~2.1–3.75 GPa for the Cu–Ta alloys) through the presence of Ta [34].

The exact role of the coarser Ta precipitates (i.e. in the Cu–10Ta-900 °C sample) is not obvious from the hardness data presented. It is expected that larger, incoherent particles would contribute only marginally to strengthening as compared to the effect of the Cu matrix grain size [16,45–47]. Further, the coarsening kinetics of Ta at higher temperatures (900 °C) may actually limit the volume fraction of small, coherent particles in the 10% samples as the temperature increases. This, in turn, may actually decrease the strength of the sample. However, this is not the case for low temperatures and/or lower Ta concentration samples, where the growth of these small Ta precipitates is kinetically hindered. This is supported by the extremely high hardness and mechanical properties exhibited by the Cu–10Ta-700 °C. Recall that this sample has a mean grain size of 70 nm and a much smaller average Ta particle size compared to the Cu–10Ta-900 °C sample. The Cu–10Ta-700 °C exhibits a hardness value of 3.75 GPa (see Table 1), which is significantly higher than both the Cu–1Ta-700 °C and Cu–10Ta-900 °C samples; this is almost three times that of nanocrystalline pure Cu of the same grain size. Though counterintuitive at first, this demonstrates the remarkable efficiency at which a smaller Ta particle volume fraction can strengthen the Cu matrix, well above what could be provided by Hall–Petch strengthening alone.

3.2.2. Quasi-static and dynamic compression testing

Fig. 6 shows the compression test curves, (a) quasi-static ($8.0 \times 10^{-4}\ s^{-1}$) and (b) dynamic ($4.0 \times 10^{3}\ s^{-1}$), for all

Table 1
Microstructure statistics of the ECAE consolidated Cu–Ta alloys.

Property	Statistic	Cu–1Ta-700 °C		Cu–10Ta-900 °C		Cu–10Ta-700 °C	
Cu grain size	Mean	168		213		70	
	SD	53		67		25	
	Min	79		75		24	
	Max	362		513		178	
	Count	113		245		240	
		<30 nm*	>30 nm	<30 nm	>30 nm	<30 nm	>30 nm
Ta particle size	Mean	11	-	17	122	7	40
	SD	4	-	7	55	4	15
	Min	5	-	6	37	2	17
	Max	29	-	36	267	17	111
	Count	235	-	87	152	87	127

* 30 nm was chosen as the demarcation point for the observed bimodal particle size distribution. All units in nm except for counts.

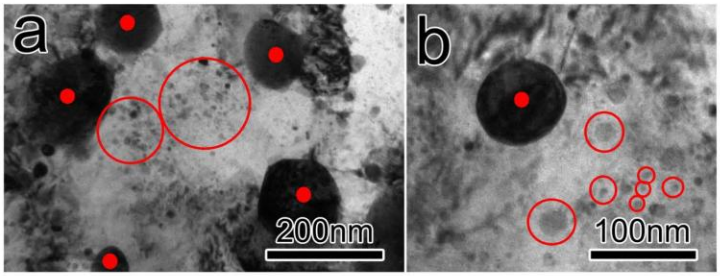

Fig. 5. High-magnification bright-field TEM images of Cu–10Ta-900 °C, showing the nature of the bimodal Ta particle size distribution with (a) coarser particles and (b) considerably finer particles or clusters. There is an about tenfold size difference between the two sets of particles.

Table 2
Mechanical properties (GPa) of the ECAE consolidated Cu–Ta alloys along with nanocrystalline copper and tantalum [34,51–53,56,57].

Property	Symbol	Cu–1Ta 700 °C	Cu–10Ta 900 °C	Cu–10Ta 700 °C	NC pure Cu	NC pure Ta
HV		2.12	2.12	3.75	2.55 1.35 1.05	4.10[d] 2.50[d]
HV/6		0.35	0.35	0.62	0.43 0.23 0.18	0.68 0.42
	σ_{ys}	0.40	0.39	0.65	0.33[b]	–
SPT	σ_{us}	0.43	0.45	0.69	0.42[b]	–
	α	1.75	1.71	1.69	1.77[b]	–
HV/3		0.70	0.70	1.23	0.85 0.45 0.35	1.36 0.83
QS	σ_{ys}	0.70	0.66	1.10	0.80[a] 0.45[a] 0.35[a]	1.30[e] 0.90[e]
	$\sigma_{0.1}$	0.80	0.80	1.29	–	1.60 0.95
DY	$\sigma_{0.1}$	0.99	0.99	1.47	0.88–0.55[c]	2.00 1.20[f]

The mechanical properties listed are from Vickers hardness testing (HV), shear punch testing (SPT), quasistatic compression testing (QS) and dynamic compression, Split–Hopkinson bar testing (DY). HV/3 and HV/6 correlate with compression and shear yield strengths (σ_{ys}), respectively. α is the ratio of the yield strength in quasistatic compression tests to that in shear punch tests. The ultimate stress and flow stress at 10% strain are represented as σ_{us} and $\sigma_{0.1}$, respectively.

[a] Nanocrystalline pure Cu: QS σ_{ys} [34]. Values for HV, HV/3 and HV/6 are converted from the given yield values. The grain sizes for these values are 5, 70 and 250 nm, respectively.

[b] Nanocrystalline pure Cu: SPT data [51]. Grain size for the reported electrodeposited nanocrystalline Cu is 74 nm.

[c] Nanocrystalline pure Cu: DY $\sigma_{0.1}$ [52,53]. Grain sizes for these values are ~35 and ~300 nm.

[d] Nanocrystalline pure Ta: HV [56]. Values for HV/3 and HV/6 are converted from the given HV values. Grain sizes for these values are 56 and 160 nm, respectively.

[e] Nanocrystalline pure Ta: QS σ_{ys} and $\sigma_{0.1}$ [56,57]. Grain sizes for these values are 44 and 250 nm.

[f] Nanocrystalline pure Ta: DY $\sigma_{0.1}$ [56,57]. Grain sizes for these values are 44 and 250 nm.

three ECAE-consolidated Cu–Ta alloy samples. Table 2 also includes the compression test data for Cu–Ta samples tested at these strain rates. At both strain rates, the yield stresses of Cu–10Ta-900 °C and Cu–1Ta-700 °C are comparable, and support our earlier observations in terms of the grain size and hardness. More specifically, comparing the behavior at both rates, the Cu–10Ta-900 °C sample shows a slow and continuous (almost elastic perfectly plastic) strain-hardening behavior with increasing plastic strain. This can be attributed to the presence of the large (500 nm) grains, which may accommodate a small amount of strain hardening. Initially, within the first 2% of strain, the Cu–1Ta-700 °C sample exhibits slightly more strain hardening, which is followed by a more constant stress region, but is still very similar to the Cu–10Ta-900 °C sample.

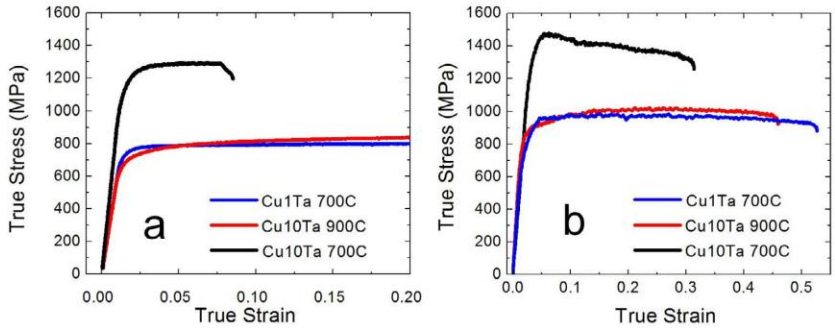

Fig. 6. True stress–true strain compression curves for the three alloy samples, Cu–1Ta-700 °C, Cu–10Ta-900 °C and Cu–10Ta-700 °C, at (a) quasistatic (8.0×10^{-4} s^{-1}) and (b) dynamic strain rates (4.0×10^{3} s^{-1}). The Cu–1Ta-700 °C and Cu–10Ta-900 °C samples exhibit similar strength and plasticity values at both strain rates, while the Cu–10Ta-700 °C sample is considerably stronger, but with less plasticity.

In contrast, similar to that observed in the hardness data, the Cu–10Ta-700 °C sample has much higher yield strengths at both strain rates. At the onset of plasticity, there is a small amount of rapid transient strain hardening, followed by a pronounced strain-softening behavior, especially at the dynamic rate. Additionally, in terms of plastic deformation beyond yield, the Cu–10Ta-700 °C sample has a significantly lower amount of compressive plasticity in contrast to the Cu–10Ta-900 °C and Cu–1Ta-700 °C samples.

Previous studies suggest that a fine grain size can lead to a limited amount of dislocation-based deformation in most metals [34,48,49], including Cu. Recent work on confined cryorolling of nanocrystalline Ni (grain size ~20 nm) indicates strong strain-hardening behavior due to the profuse formation of Lomer–Cottrell locks [50]; this is because confined rolling rules out the possibility of tensile instability, which would otherwise be the primary reason for the absence of strain hardening in nanocrystalline metals. Earlier reports on nanocrystalline Cu with a grain size below 100 nm have also shown either a limited strain-hardening behavior right after the yield point or no strain hardening at low strain rates, due both to a rapid saturation of dislocation activity in the material and to the early onset of plastic instability, which leads to premature fracture of the specimen. However, at dynamic strain rates, the strain-softening behavior is more pronounced, and is likely attributable to dynamic recovery or the associated adiabatic temperature rise. The melting point, T_m, of Cu is 1083 °C (1356 K), and even a slight temperature rise above ambient conditions (i.e. 300 K) represents a nominally high homologous temperature (for Cu, this is about ~1/4 T_m). The calculation of the adiabatic temperature rise is more significant if there is also an increase in material strength and total ultimate strain; in the case of Cu–10Ta-700 °C, this rise in properties could be caused by the much smaller grain size of the Cu matrix.

The compressive properties of the ECAE-processed Cu–Ta samples are much higher than those of the pure nanocrystalline Cu samples (see Table 2). The strength of pure Cu for a grain size of 70 nm is 450 MPa, and the strength for a grain size of 250 nm is 350 MPa [34]. The other data points in the table are for pure Cu under different conditions, which are taken from relevant references [34,51–57]. As shown in the table, the Cu–10Ta-900 °C and Cu–1Ta-700 °C samples show modest increases of a few hundred megapascals compared to nanocrystalline pure Cu of the same grain size. However, the Cu–10Ta-700 °C sample (70 nm grain size) has a yield strength of ~1100 MPa (more than a 100% increase over that of pure Cu). Thus, when the minor effect of strengthening provided by the grain size difference from 70 to 250 nm (~100 MPa, Hall–Petch relation) is considered, there is a much greater amount of hardening in the Cu–10Ta-700 °C sample, which cannot be accounted for by Hall–Petch strengthening alone. Again, this analysis indicates that the strength increase is related not only to the Cu matrix grain size, but also to the Ta precipitates; their role on the strength of the matrix must also be considered.

Another observation may be made from the quasi-static and dynamic stress–strain curves of these three samples; they all show a significant strain rate dependence. A more quantitative description of the strain rate dependence and the activation volumes associated with the plastic deformation of these samples will be provided subsequently. Under dynamic loading, all specimens exhibit either an elastic–perfectly plastic behavior (Cu–1Ta-700 °C and Cu–10Ta-900 °C) or a flow-softening behavior (Cu–10Ta-700 °C). We believe that this is due to the adiabatic temperature rise during dynamic loading, where the time frame is so short that the heat generated from mechanical work cannot diffuse out of the specimen. Usually, the following equation can be used to estimate the adiabatic temperature rise during dynamic loading:

$$\Delta T = \frac{\beta}{\rho c_p} \int_0^{\varepsilon_f} \sigma d\varepsilon \tag{3a}$$

For the specimens of this work that exhibit elastic–perfectly plastic behavior, Eq. (3a) reduces to

$$\Delta T = \frac{\beta}{\rho c_p}\sigma \cdot \varepsilon_f \tag{3b}$$

In Eqs. (3a) and (3b), ΔT is the adiabatic temperature rise, β is the fraction of mechanical work converted into heat (i.e. Taylor–Quinney factor [58]), usually taken to be 0.9 for Kolsky bar experiments, ρ is the mass density (8.9 g cm^{-3} for Cu), c_p is the specific heat (24.43 J K^{-1} mol^{-1} for Cu), σ is the flow stress, and ε_f is the final strain. For example, for Cu–10Ta-700 °C, a final strain of 0.3 results in a temperature rise of ~110 K. This temperature rise, especially for Cu, translates into considerable thermal softening of the specimen. We believe that this simple estimation explains in part the difference between the quasi-static and dynamic flow behaviors. That is, under quasi-static uniaxial compression, the samples still exhibit some strain hardening, whereas under dynamic compression, strain hardening has been outpaced by (adiabatic) thermal softening within the sample.

3.2.3. Shear punch testing

Fig. 7 shows the representative SPT curves for all of the ECAE-consolidated Cu–Ta samples, and Table 2 summarizes the yield and ultimate strengths obtained from the SPT curves, as well as those properties measured in compression. At relatively low strain rates, the SPT data follows the relationship $\sigma = \alpha\tau_{SPT}$, where σ, τ_{SPT} and α are the tensile/compressive strength, shear strength and a correlation factor, respectively. In the literature, α values have been reported to vary between 1.35 and 1.8, depending on the test setup parameters employed. Earlier studies reported an α value of 1.71 in different metal and alloy systems [27]. The data presented in Table 2 also indicates a σ/τ_{SPT} ratio of ~1.7, given a compressive yield strength measured at a strain rate of 8×10^{-3} s^{-1} and the corresponding SPT yield strength in shear. It is noted that the SPT data also follows the compression test data trends for the Cu–Ta samples. The yield strengths of the Cu–1Ta-700 °C and Cu–10Ta-900 °C samples are comparable; the Cu–10Ta-700 °C sample has the highest yield and ultimate strengths. Similar to the compression curves, the Cu–10Ta-900 °C sample has a higher degree of strain hardening than the Cu–1Ta-700 °C sample, and the Cu–10Ta-700 °C sample has limited strain hardening within the first couple per cent displacement. The behavior of the latter could be due to the finer grain size compared to the other two samples.

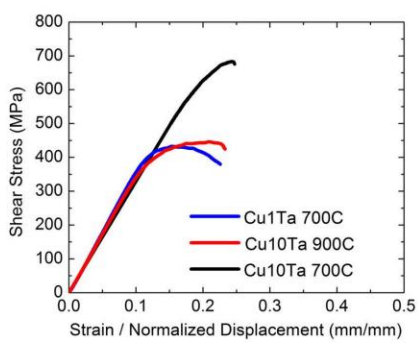

Fig. 7. SPT curve results of the three alloys, Cu–1Ta-700 °C, Cu–10Ta-900 °C and Cu–10Ta-700 °C. The observed trends are similar to those obtained in compression. There is a greater drop in shear stress for the Cu–1Ta-700 °C sample, reflecting the more brittle nature of this specimen.

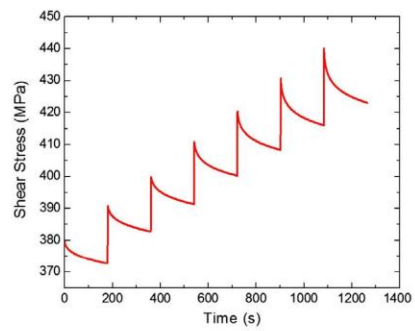

Fig. 8. Type I stress relaxation test profile performed on the Cu–1Ta-700 °C and Cu–10Ta-900 °C samples. In the case of the Type I relaxation test, the shear stress is ramped to increasingly higher levels (380–440 MPa, with 10 MPa increments) and allowed to relax for a fixed time interval (180 s) at each stress.

Both types of stress relaxation tests were performed on the ECAE-consolidated Cu–Ta samples. Fig. 8 shows the Type I stress relaxation test profile conducted on the Cu–10Ta-900 °C and Cu–1Ta-700 °C samples. A similar relaxation test was conducted on the Cu–10Ta-700 °C sample, but its brittle nature caused problems with the Type I and Type II relaxation tests. Therefore, no further tests were conducted with this sample.[2]

The activation volume can be calculated from the resultant stress relaxation data. The magnitude of the stress drop in the Type I stress relaxation curve follows a logarithmic dependence as a function of time [59], i.e.

$$\Delta\tau = -\frac{kT}{V_r}\ln\left(1 + \frac{t}{c}\right) \tag{4}$$

where $\Delta\tau$ is the shear stress decrement during the stress relaxation process (<0), V_r is the apparent activation volume, t is the time of stress relaxation and c is a time constant. For Cu, at an ambient test temperature (i.e. 300 K), $kT/b^3 = 247$ MPa [16], where b is the Burgers vector of Cu. Usually, in tensile or compression tests of polycrystalline cubic metals, a Taylor factor value of ~3.0 is used to convert the normal yield stress to the critical resolved shear stress, i.e. $\sigma = 3\tau_r$ [16]. Along with the experimentally obtained correlation of $\sigma = 1.7\tau_{SPT}$, it provides a relationship between the shear strength obtained from the

[2] See how the data in Fig. 8 show a drop in the shear stress with respect to time.

shear punch test and the critical resolved shear stress, $\tau_{SPT} = 1.764\tau_r$. Rearranging Eq. (4) then results in

$$\Delta\tau_{SPT}/1.764 = -\frac{kT}{V_r}\ln\left(1+\frac{t}{c}\right) \quad (5)$$

The apparent activation volume values, V_r, obtained using Eq. (5) after each relaxation while increasing the stress levels above the yield point, are shown in Fig. 9 for the ECAE-consolidated Cu–Ta samples. Data for coarse-grained pure Cu is also included in the figure for comparison.

The data clearly indicates a difference in activation volume between the Cu–1Ta-700 °C and Cu–10Ta-900 °C samples. For instance, although the yield strengths are comparable (within 15 MPa; see Table 2), in the very first relaxation, at a stress level just above the yield stress, the relaxation responses are very different. This shows clear evidence of reduced dislocation activity with a decreased grain size. After the initial relaxation, the decrease in the activation volume in subsequent relaxation tests (i.e. higher stress levels) suggests that all samples undergo a small degree of strain hardening.

The Type II stress relaxation tests were also performed on the ECAE-consolidated Cu–Ta samples. Fig. 10 shows an example of the Type II stress relaxation tests conducted

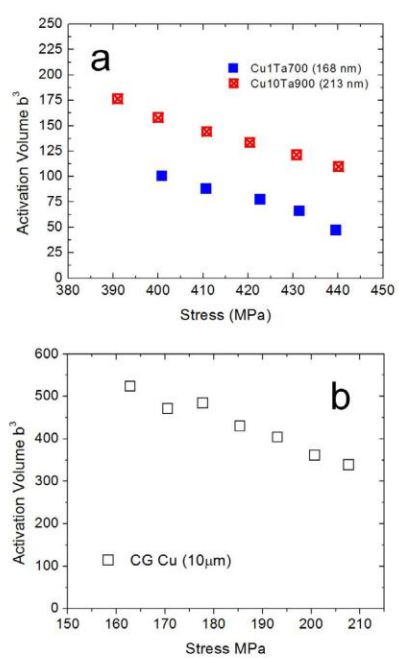

Fig. 9. Apparent activation volume V_r as a function of the applied stress for (a) the Cu–1Ta-700 °C and Cu–10Ta-900 °C samples and (b) the coarse-grained Cu sample. The coarse-grained Cu has a much higher activation volume at significantly lower stresses as compared to the nanocrystalline Cu–Ta samples.

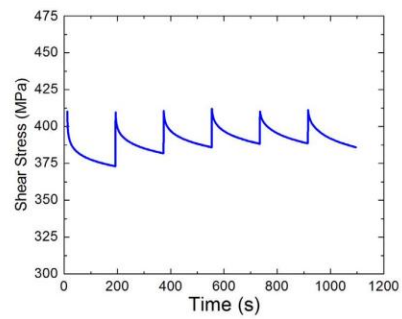

Fig. 10. Type II stress relaxation test performed on the Cu–10Ta-900 °C and Cu–1Ta-700 °C samples. Unlike those of the Type I stress relaxation conditions (increasing stress), the shear stress in the Type II test is ramped to a constant stress (410 MPa), then allowed to relax for a fixed time interval (180 s).

on the Cu–1Ta-700 °C sample; similar tests were conducted on the Cu–10Ta-900 °C sample as well. The Type II stress relaxation tests are conducted with repeated relaxations after reloading back to the initial stress value (but not exceeding it).

The physical activation volume V^* was obtained from the relation [59,60]:

$$V^* = \frac{kT}{\tau_{j+1}^{initial} - \tau_j^{final}}\ln\left(\frac{\dot{\gamma}_{j+1}^{initial}}{\dot{\gamma}_j^{final}}\right) \quad (6)$$

where $\dot{\gamma}_j^{final}$ is the plastic strain rate at the end of relaxation j and $\dot{\gamma}_{j+1}^{initial}$ is the rate at the start of the next relaxation, $(j+1)$; τ_j^{final} and $\tau_{j+1}^{initial}$ represent the corresponding critical resolved shear stresses. The shear strain rate, $\dot{\gamma}$, at any time, t, for a given stress relaxation test can be calculated by [30,59]:

$$\dot{\gamma} = \frac{kT}{MV_r}\frac{1}{t+c} \quad (7)$$

using the values of V_r and c, which were already determined from Eq. (4), as well as the combined machine-specimen modulus M. Note that, for determining V^*, measuring M is not required in Eq. (7), because the ratio of the strain rates cancels out this term.

The physical activation volume V^* can now be calculated for the ECAE-consolidated Cu–Ta samples. This activation volume represents the average volume of dislocation structure involved during deformation, which is a real signature of the underlying mechanism responsible for the plastic deformation, with a definite value and stress dependence representing each atomistic process.

Fig. 11 shows the V^* values derived from the Type II stress relaxation tests for the Cu–1Ta-700 °C and Cu–10Ta-900 °C samples as a function of relaxation number/sequence. For the Cu–1Ta-700 °C sample, V^* is about $41b^3$; for the Cu–10Ta-900 °C sample, V^* is about $53b^3$. Due to its poor ductility, the Cu–10Ta-700 °C sample was not tested. The data from the coarse-grained Cu

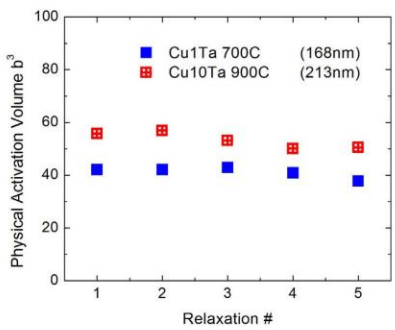

Fig. 11. Physical activation volume V^* for the Cu–1Ta-700 °C and Cu–10Ta-900 °C samples. The physical activation volume is relatively constant with the number of stress cycles. The activation volumes for the two samples are similar, indicating that the deformation mechanisms in the samples are more dependent on the Cu grain size than the size distribution of the Ta precipitates.

sample is not shown here since only one or two relaxations would be obtainable prior to saturation. The Type II stress relaxation test provides complementary information to the more typical strain rate jump test. In the latter, the physical activation volume is obtained from differences in the relaxation strain rate with increase in stress for a fixed microstructural state and mobile dislocation density. Note that Fig. 11 indicates a relatively constant value for V^*, i.e. the physical activation volume is independent of the test cycle number.

4. Discussion

The synthesis of forced solid-solution Cu–Ta alloys has been shown to form well-dispersed nanoscale composite structures as a result of ECAE consolidation at high temperatures [5,9]. Table 2 provides a direct comparison of the attained mechanical properties of the three alloy compositions to those of pure nanocrystalline Cu and Ta taken from literature. Most intriguing is that, for each case, the Cu–Ta alloys far exceed the properties of pure Cu, even those with grain sizes much smaller than 10 nm. As an example, Fig. 12 shows a Hall–Petch plot of yield stress as a function of the inverse square-root of grain size for a number of nanocrystalline Cu samples compiled in a recent review of nanocrystalline Cu [61] along with the present nanocrystalline Cu–Ta results. In this plot, the as-milled Cu–Ta sample at 6 nm is an estimate of the yield stress based on the Vickers hardness [5]. All four nanocrystalline Cu–Ta samples deviate from the nanocrystalline Cu results, which plateau at stresses on the order of 900 MPa for grain sizes below 25 nm. Certainly, in the case of the 70 nm grain size for the Cu–10Ta-700 °C and the as-milled Cu–Ta sample, there is a significant increase in yield stress over even the smallest grain sizes for nanocrystalline Cu. This plot also indicates that strengthening due to grain size is not the only predominant strengthening mechanism operating in these ECAE-consolidated nanocrystalline Cu–Ta samples.

The effect of these small Ta additions clearly constitutes an increased level of strengthening in nanocrystalline Cu. The mechanical properties are so impressive that, with the addition of only 10% Ta, they are comparable to those of nanostructured pure Ta [56] (Table 2). It was shown that small changes in the grain size induced by the ECAE temperature only have a minimal effect on mechanical properties, but the resultant change in the Ta particle size significantly alters the strength of the Cu–Ta alloy. Therefore, in the following section we discuss the significant influence of these Ta precipitates on the properties and behavior of the consolidated nanocrystalline Cu–Ta specimens.

4.1. Particle interactions in strengthening of metals

Our study reveals that the Ta particle distribution and morphology vary with composition and consolidation temperature, which also contributes to the material strength. These particles are observed to range in size from small (particle diameter less than 10 nm) to medium (particle diameter between 10 and 50 nm) and large (particle diameter greater than 50 nm). As such, the Ta particles dispersed throughout the matrix can strengthen the material in several ways. Fine coherent particles can act as barriers for dislocations, increasing the shear stress required for dislocation motion as the dislocations glide through the matrix (and cut through the particles) [33]. On the one hand, it is easier for dislocations to sweep through a material with smaller second phase particles. However, as the particle size increases, it becomes increasingly more difficult for dislocations to glide through the matrix. On the other hand, these larger, more impenetrable Ta particles can force dislocations to move through the lattice by only bowing between the particles, i.e. via the Orowan strengthening mechanism. The volume fraction of these larger particles play an additional role through a rule of mixtures hardening, in which the composite property is a weighted average of the respective volume fractions of the two phases. Thus, for smaller particles, increasing Ta particle size increases the stress required for dislocation cutting. Conversely, increasing the particle size decreases the stress required for dislocation bowing. Therefore, there is an optimal particle size for material strengthening.

4.2. Effect of Ta in strengthening nanocrystalline Cu

There exists a particle with a critical radius r_c that can no longer be sheared through by dislocations. This dimension can be found by equating the shear stress required for a dislocation cutting through the particle to the shear stress required for a dislocation bowing around it. An elegant treatment of this problem by Friedel leads to the following equation [62]:

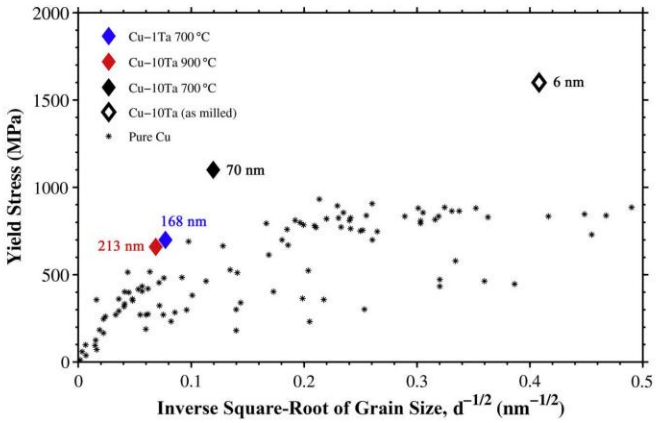

Fig. 12. Hall–Petch plot of pure copper (data was taken from several sources compiled in a recently published review article on nanocrystalline copper [61] vs. data for Cu–Ta alloys). The red, blue and black data points correspond to the alloys discussed in the current article, while the open diamond (6 nm) represents the expected yield as estimated by Vickers hardness measurements reported in Ref. [5]. The plot demonstrates clearly the large degree of strengthening Ta imparts to the Cu matrix over and above what is possible by grain size alone. (For interpretation of the references to colour in this figure legend, the reader is referred to the web version of this article.)

$$r_c = \alpha \frac{Gb_2}{\gamma} \tag{8}$$

In Eq. (7) α is on the order of unity and γ is the interfacial energy between Cu and Ta (a coherent interface is assumed). Applying this to the Cu–Ta alloys, where $G = 48$ GPa, $b = 0.255$ nm (Burgers vector for fcc Cu) and $\gamma = \sim 100$ mJ m^{-2} [63], results in a critical diameter of ~30 nm. Thus, the large- to medium-sized Ta particles can be considered non-shearable. It is well known that, if such particles reside in the lattice of the matrix phase, dislocation loops would accumulate around these particles upon loading. This is the classical Orowan strengthening mechanism, where incoherent particles in the matrix force dislocations to move around them, leaving behind dislocation loops [33]. However, this mechanism has a minimal effect on increasing the yield point, though it dramatically enhances strain hardening through dislocation accumulation. In the present study, strain hardening was not observed in the Cu–Ta specimens (i.e. there is minimal, if any, Orowan strengthening; see Fig. 6), suggesting that the impressive strengths of these nanocrystalline alloys stem from grain size effects, rule of mixtures effects and interactions between small Ta clusters/precipitates with the surrounding microstructure.

4.2.1. Strengthening from rule of mixtures and Hall–Petch mechanisms

The various strengthening contributions can be delineated based on the assumption that various effects contribute additively to the overall strength of the nanocrystalline Cu–Ta specimens. For instance, the relative contributions of each of these strengthening effects may be computed for the three samples (Cu–1Ta-700 °C, Cu–10Ta-900 °C and Cu–10Ta-700 °C). While prior studies have attempted to deconvolute simultaneously operating mechanisms that contribute to the overall strength [16], it should be noted that these mechanisms may interact with each other, giving rise to a much higher strengthening efficiency. In the following subsections, quantifying the potential contributions of well-known strengthening mechanisms, such as rule of mixtures and grain size (Hall–Petch) effects, may provide further insight on the relative strengthening mechanisms that lead to the unprecedented strength of nanocrystalline Cu–Ta alloys.

First, the rule of mixtures strengthening effect was evaluated for the Cu–Ta samples. In the Cu–Ta samples reported here, many of the larger Ta particles reside at grain boundaries and are comparable in diameter to the matrix grain size. The exception is the Cu–10Ta-900 °C sample, where a small volume fraction of the microstructure contains grains with diameters of >200 nm. Therefore, the larger Ta particles are considered to contribute to strengthening through the rule of mixtures only, as they do not reside in the Cu lattice and are large relative to the Cu matrix grain size. Furthermore, such precipitates should not play a role in defining the activation volume either, since their size and spacing are on the order of the matrix grain size. Additionally, such composite hardening has been shown to only moderately contribute to increases in strength compared to that attained by the Hall–Petch effect [16,45–47]. Table 3 lists the rule of mixtures strengthening contributions for the Cu–Ta alloys herein. At most, the rule of mixture strengthening accounts for ~25% of the experimentally measured hardness values. In the calculations of strengthening effects for Cu–Ta alloys, the global Ta content is assumed to be dispersed as a large composite phase (upper limit of rule of mixtures effect). Consequently,

Table 3
Strengthening effects in the ECAE consolidated Cu Ta alloys.

Cu Alloy	Experimental hardness (GPa)	Strengthening mechanism contributions, GPa (% of total)			
		Rule of mixtures	Hall Petch	Combined (ROM + H P)	Other
Cu 1Ta-700 °C	2.12	0.047 (2%)	0.880 (42%)	0.927 (44%)	1.193 (56%)
Cu 10Ta-900 °C	2.12	0.465 (22%)	0.790 (37%)	1.255 (59%)	0.865 (41%)
Cu 10Ta-700 °C	3.75	0.388 (10%)	1.322 (35%)	1.710 (46%)	2.040 (54%)

the volume fractions for 10% and 1% Ta in Cu are 14.5% and 1.5%, respectively. Furthermore, a Ta particle hardness of 4.1 GPa [56] is used in these calculations; this assumes that the Ta particles have a diameter of approximately 40 nm. Therefore, the maximum possible rule of mixtures hardening contributions from the Ta particle dispersions for Cu–1Ta-700 °C, Cu–10Ta-900 °C and Cu–10Ta-700 °C are 0.047, 0.465 and 0.388 GPa, respectively (Table 3).

Second, the grain size strengthening (Hall–Petch relationship, i.e. $kd^{-1/2}$) was evaluated for the Cu–Ta samples. The hardness of the Cu matrix phase is calculated based on the grain size d as measured by TEM with a Hall–Petch slope of $k = 0.11$ MN m$^{-3/2}$. For the three samples, the calculated Cu matrix grain sizes are 168, 213 and 70 nm, respectively. The corresponding hardenings from the Hall–Petch relationship are therefore 0.880, 0.790 and 1.322 GPa, respectively. Table 3 lists these values; note that the Hall–Petch strengthening accounts for ~40% of the experimentally measured hardness. Interestingly, if the rule of mixtures and Hall–Petch effects are combined, the total possible hardenings from Cu grain size and Ta particle effects alone for Cu–1Ta-700 °C, Cu–10Ta-900 °C and Cu–10Ta-700 °C are 0.927, 1.255 and 1.710 GPa, respectively. Subtracting these values from the as-consolidated sample hardness values (2.12, 2.12 and 3.75 GPa) results in differences of 1.193, 0.865 and 2.040 GPa, respectively (listed as "Other" in Table 3).

These differences indicate that a significant residual strengthening effect remains unaccounted for in the samples, which is on the order of the Hall–Petch and rule of mixtures strengthening contributions combined. It is expected that this residual strengthening arises from small Ta particle and cluster contributions, which are a very efficient strengthening mechanism in the nanocrystalline Cu–Ta samples. Some authors have calculated Orowan strengthening as an additional strengthening mechanism; however, this is often a smaller effect than the strengthening due to grain size [16]. Once again, the lack of matrix particle sizes required for Orowan strengthening and the absence of observed strain hardening in the present study clearly show that Orowan strengthening has a marginal, if any, role in strengthening the reported nanocrystalline Cu–Ta alloys. Therefore, additional strengthening to the Cu–Ta alloys must come from other strengthening sources, such as grain boundary strengthening from Ta solutes (Section 4.2.2), strengthening from small-scale coherent Ta particles and clusters (Section 4.2.3) and composite effects related to the interaction of Ta with other strengthening mechanisms (Section 4.2.4).

4.2.2. Grain boundary strengthening from Ta solutes

Fig. 4b and c suggests that a bimodal Ta particle size distribution exists for Cu–10Ta-900 °C and Cu–10Ta-700 °C. As stated earlier, the majority of the larger Ta particles (>30 nm) are almost always observed at grain boundaries. It is suggested that this dichotomy exists due to Ta GB diffusion, which promotes continued growth of Ta particles. This observation is consistent with other reports of coarsening, where phase separation in immiscible nanocrystalline Cu alloys is thought to occur by GB diffusion of solute atoms [2]. This scenario does not exist in the lattice, where diffusion of Ta within Cu lattice is difficult even at temperatures nearing the T_m of Cu [9]. Thus, in the Cu–10Ta-900 °C and Cu–10Ta-700 °C samples, the larger particles of the bimodal distribution exist on or near GBs and therefore do not hinder dislocation motion significantly. Recently, the GB engineering concept due to the presence of select solutes within the GBs has been used to explain the dramatically increased strength levels observed in nanocrystalline metals [8]. Seah's analysis of constituent elements that could cause GB decohesion (and cohesion) suggests this same argument [64]. Though Seah studied the effects in conventional, coarse-grained alloys, such cohesive effects should be amplified in nanocrystalline alloys, where a much larger volume fraction of GBs exists. That is, Ta at Cu GBs acts as a potent agent for increasing GB cohesion. Alternatively, GB activities such as grain boundary sliding have been proposed for the plastic deformation of nanocrystalline Cu [65]; the presence of these Ta particles at GBs will naturally increase the barrier strength for such GB activities. As a consequence, the strength of the composite material is expected to significantly increase.

4.2.3. Strengthening from small-scale Ta particles and clusters

Small or coherent particles are known to dramatically increase the yield stress of materials. However, upon reaching and exceeding the yield stress, these small barriers are eventually passed or sheared through via a mechanism similar to that which shears Guinier–Preston zones [33]. It was shown in the prior analysis that all Ta particles dispersed within the Cu matrix are sufficiently fine that they can be considered shearable. This type of hardening mechanism has a minimal impact on strain hardening and can result

in a decline in yield stress after dislocations shear through such fine particles [33]. Once sheared, the dislocations break away and move relatively freely through the rest of the lattice until the next strong barrier is reached. Some recent experiments have shown that annealing ion-plated nanocrystalline Cu–Ta thin films at temperatures as high as 900 °C results in the as-fabricated solid solution decomposing into a fine dispersion of Ta particles [66]. A large fraction of these particles with a size range below 8 nm retained a face-centered cubic structure and were coherent with the Cu matrix. The current study, along with data reported previously [5], indicates that such fine Ta precipitates exist and could account for the majority of Ta dispersed in the Cu matrix.

While the volume fraction of these small Ta particles changes with both composition and processing temperature, it ultimately determines the overall mechanical properties of the nanostructured Cu–Ta samples. For instance, when comparing the three ECAE-consolidated Cu–Ta samples (Cu–1Ta-700 °C (168 nm grain size), Cu–10Ta-900 °C (213 nm grain size) and Cu–10Ta-700 °C (70 nm grain size)), the 1% Ta sample has a lower volume fraction of particles. However, these particles are all very small relative to those in the 10% Ta samples. When comparing the two 10% Ta-containing samples, the contribution to stress from the grain size difference alone (70 vs. 213 nm) is only ~100 MPa (based on pure nanocrystalline Cu [34]). Therefore, there still exists a large disparity in mechanical properties that can only be explained by the difference in the Ta particle sizes.

4.2.4. Composite effect of Ta on strengthening Cu

Given the above discussion, the following scenario of Cu strengthening by Ta is hypothesized. First, there is a significant volume fraction of small particles (typically less than 10–15 nm) that are dispersed within the Cu matrix. These Ta particles may have coherent interfaces with the Cu matrix phase, depending on their size. Such particle dispersions can cause large increases in strength, but provide little or no strain hardening, since they would be cut by dislocations at yielding. Second, there are a number of much larger Ta particles as well. These only contribute to strengthening through a rule of mixtures hardening. Third, as the ECAE consolidation temperature is changed, these larger particles can coarsen; the Ta particle size increases with increasing temperature through GB segregation and diffusion of Ta atoms. It should be noted that higher processing temperatures will most likely increase the Cu grain size as well. Moreover, at higher processing temperatures (e.g. >900 °C), this combination of larger Ta particle size and Cu grain size may elevate the level of Orowan strengthening. However, this is not the case at intermediate temperatures (~700 °C). For instance, the Cu–10Ta-700 °C and Cu–1Ta-700 °C samples have a combination of smaller Cu grains and much finer dispersions of Ta particles, which are easily cut through or thermally bypassed, all of which are not conducive to Orowan strengthening (i.e. accumulating and storing dislocations). However, both small grain size and small particle size are effective at dramatically increasing the strength of the matrix to resist deformation, but do not necessarily alter the dislocation mechanism operating during plastic deformation.

There are a number of challenges that make separating and quantifying the various strengthening mechanisms in the present nanocrystalline Cu–Ta alloys and other binary nanocrystalline systems difficult. First, as experimental processing parameters are varied, there is extensive coupling of the various microstructure features that makes it difficult to identify the role of any one strengthening mechanism in this system. For instance, as has been discussed previously, increasing/decreasing the ECAE temperature will not only modify the size distribution and volume fraction of the small of Ta precipitates, but will also modify the size distribution and volume fraction of large Ta particles, the amount of Ta that segregates to the grain boundaries, the copper grain size and the potential interaction between these microstructure changes. Furthermore, these changes in the Cu–Ta microstructure may potentially result in modifying or generating new strengthening mechanisms. For example, the grain size of the nanocrystalline Cu–Ta alloys is in a regime where dislocation nucleation from grain boundaries is expected to be one of the dominant mechanisms. It is not clear what effect Ta within the grain boundary or nearby Ta clusters may have on nucleating dislocations or storing/transmitting existing dislocations. Also, the role that dislocation nucleation and interfacial dislocations at the interface between Cu grains and large Ta particles play in strengthening nanocrystalline Cu–Ta is not known. Moreover, the atomic size and thermal expansion mismatch between Cu and Ta may result in residual strain within the lattice, whether Ta is located as small precipitates in the center of grains or located at the boundaries. In this respect, utilizing molecular dynamics and other simulation techniques at the nanocrystalline grain scale level will provide further insight into the magnitude and importance of the multiple potential strengthening effects that Ta plays in strengthening nanocrystalline Cu–Ta.

4.3. Defining the activation volume of nanostructured Cu–Ta alloys

The activation volume represents the average volume of the dislocation event involved in the plastic deformation process. As pointed out by Taylor [67], the physical image of the activation volume of plasticity is the average volume swept by dislocation segments during a single dislocation motion event. As such, it is a fingerprint of the plastic deformation mechanism. More importantly, it is directly related to the ongoing deformation mechanisms, with a definite relationship and characteristic stress dependence for each dislocation-mediated process [33,59]. In all three Cu–Ta samples, most of the small Ta precipitates do not participate in the deformation process by pinning

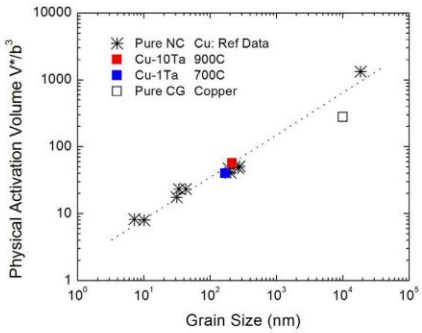

Fig. 13. Physical activation volume V^* for the Cu–1Ta-700 °C, Cu–10Ta-900 °C and coarse-grained (CG) Cu samples as a function of the grain size, as well as reported values for pure nanocrystalline Cu [51–53]. The agreement with the previous Cu data indicates that the deformation mechanism in the nanocrystalline Cu–Ta samples is similar to that observed in nanocrystalline copper.

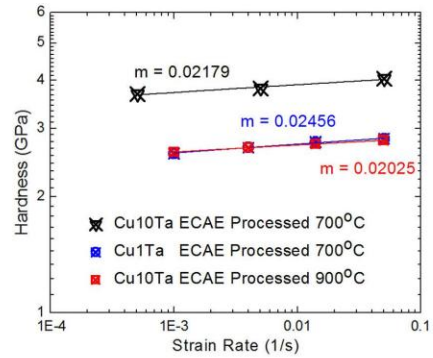

Fig. 14. Strain-rate sensitivity for the Cu–1Ta-700 °C, Cu–10Ta-900 °C and Cu–10Ta-700 °C samples based on nanoindentation measurements. The data for the Cu–Ta samples is consistent with the strain rate sensitivities of other reported CG and nanocrystalline Cu values.

dislocations, but instead are bypassed at yielding. If this fact were true, the activation volume would not be affected by the presence of small Ta particles, but would rather be defined by the Cu matrix grain size. Displayed in Fig. 13 is the measured physical activation volume (V^*) of the samples. The values of the measured physical activation volume are between $10b^3$ and $100b^3$. Included in the graph are data for coarse-grained and nanocrystalline Cu with various grain sizes. Typically, values of V^* less than $10b^3$ are associated with GB activities such as sliding and rotation, whereas values of V^* greater than $10b^3$ but less than $\sim 50b^3$ are usually believed to be associated with GB activities combined with partial dislocation activities, such as the emission of partial dislocations from a GB, and are absorbed at the opposite end of the GB. Larger values of V^* are commonly ascribed to dislocations cutting through forest dislocations as the rate-limiting mechanisms [31,60]. The transition from one distinctly different mechanism to another is still a subject of research; however, dislocation cross slip has been proposed as a possible mechanism. The activation volumes reported agree with the expected trends of grain size and activation volume obtained from the literature [29], despite the large fraction of Ta particles they possess.

As noted earlier, the activation volume and the strain-rate sensitivity are interrelated (Eq. (2)), which is an additional parameter important in determining the constitutive response of nanocrystalline metals [31]. Fig. 14 displays the strain-rate sensitivity for all three samples as measured by nanoindentation. It should be noted that both the strain rate and the hardness values are plotted on a logarithmic scale, assuming a power law strain-rate dependence. Thus, the slope of each curve is the strain-rate sensitivity of the respective specimen, i.e. $m = \partial \ln H / \partial \ln \dot{\varepsilon}$. The measured nanohardness values are slightly elevated compared to measurements made by conventional Vickers microhardness testing. However, all three samples show a linear

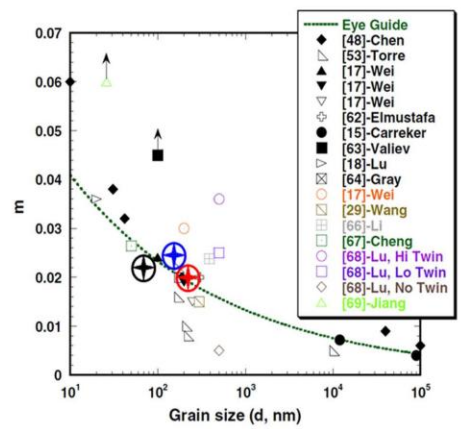

Fig. 15. Strain-rate sensitivity of various Cu samples as a function of grain size (taken from Ref. [31]), with the strain rate sensitivities of the Cu–1Ta-700 °C (blue), Cu–10Ta-900 °C (red) and Cu–10Ta-700 °C (black) samples overlaid on the graph. The strain-rate sensitivities are in good agreement with the trend line based on other reported copper samples. The author names and listed references in the legend refer to the original source document [31]. (For interpretation of the references to colour in this figure legend, the reader is referred to the web version of this article.)

response with increasing strain rate, with similar slopes. For comparison, the strain-rate sensitivity, m, of high-purity, well-annealed, coarse-grained Cu is ~ 0.004 [68,69]; for nanocrystalline Cu with a grain size of less than 30 nm, m has a value of ~ 0.04 [32,70]. A value of 0.036 for m is reported by Lu et al. for electrodeposited nanocrystalline Cu (grain size ~ 28 nm) [70]. Additionally, data in Fig. 15 demonstrate that the measured strain-rate sensitivity values for the Cu–Ta alloys agree with those of pure Cu as a function of Cu grain size. This further supports the claim that

the dominant dislocation-mediated deformation mechanism in the Cu–Ta samples is primarily dependent on the Cu matrix grain size and the Ta precipitates have a negligible role.

As an independent and more rigorous verification of our SPT measurements, the activation volumes are also calculated from the strain-rate sensitivity values. Using Eq. (2) and the average measured hardness value of each sample, the activation volumes for the Cu–1Ta-700 °C, Cu–10Ta-900 °C and Cu–10Ta-700 °C samples are $19.5b^3$, $23.7b^3$ and $15.8b^3$, respectively. At first glance, these values of activation volume appear lower than those obtained in the shear punch relaxation tests. However, the hardness values for the Cu–Ta alloys are significantly higher (by a factor of ~2) than for pure Cu of similar grain sizes. This hardness increase is attributed to the Ta particles, which are cut or bypassed at yielding. Since the activation volume is a measurement of plastic deformation processes, the Ta particles should not influence the magnitude of the activation volume itself. Therefore, using the expected hardness for the Cu matrix based on the Hall–Petch effect alone (~1.0–1.35 GPa; see Table 2) gives activation volumes of $52.8b^3$, $64.0b^3$ and $45.8b^3$, which are much closer to those measured by the shear punch relaxation tests. Regardless of the excellent agreement between the experimentally and analytically determined activation volumes, which suggest a dislocation-mediated deformation process, further research is necessary to elucidate the actual atomic scale deformation mechanisms in the bulk nanocrystalline Cu–Ta samples.

Lastly, the presence (or absence) of adiabatic shear localization is important for understanding and modeling failure mechanisms in high-strength materials under dynamic loading conditions. Herein, none of the specimens exhibited adiabatic shear localization despite their high strength and nearly diminished strain hardening. This behavior is in line with other face-centered cubic metals with ultrafine-grained and nanocrystalline microstructures [34], and is in sharp contrast to their body-centered cubic counterparts, such as W [71,72], Fe [73,74] and Ta [56]. This can be understood in the context used by Grady [75,76], who ascribed an intrinsically high "shear band" toughness compared to body-centered cubic metals to Cu. Further, the stability maps of Joshi and Ramesh [77] may be used to understand the difference between ultrafine-grained and nanocrystalline metals, such as Cu, and body-centered cubic metals. Alternatively, the numerical analysis of Guo and co-workers [78] may be used, which includes high strain rate and thermal effects. This work provides yet more evidence for the absence of adiabatic shear localization in ultrafine-grained and nanostructured Cu.

In summary, the ECAE-consolidated nanocrystalline alloys in the present study contain a variety of microstructure features that result in high levels of strengthening, as measured by quasistatic, dynamic and shear testing techniques. The activation volumes suggest dislocation mechanisms similar to conventional nanocrystalline Cu. However, the unaccounted-for strengthening beyond Hall–Petch and rule of mixtures hardening suggests that Ta plays a commanding role in strengthening the nanocrystalline Cu microstructure – up to strength levels as high as some reports for nanocrystalline Ta. While the present experimental work details the structure and mechanical properties of nanocrystalline Cu–Ta alloys, much work using experimental or simulation techniques is still needed to definitively identify the absolute strengthening mechanisms.

5. Conclusions

Nonequilibrium solid solutions between Cu and Ta, generated though high-energy cryogenic milling, decompose during ECAE consolidation, resulting in an extremely stable bulk nanostructured alloy. The observed phase separation is a function of both the processing temperature and the Ta concentration. The microstructural evolution produces a wide range of Ta particle sizes, ranging from atomic clusters to much larger precipitates. Ta particles occupying GB positions were observed to be significantly larger than particles trapped in the lattice, giving rise to a bimodal particle size distribution. This dichotomy exists due to the differences in diffusion rates of Ta atoms along GBs and through the Cu lattice, which is extremely slow even at temperatures near the T_m of Cu.

Such a distribution of Ta particles lends itself to a complex range of hardening mechanisms, operating simultaneously, which significantly strengthen the Cu matrix. It was determined that small Ta cluster/particles (with sizes of <30 nm) contribute to the majority of the observed strength increase with a marginal increase related to a rule of mixtures hardening by Ta. While the total strength of the alloy comes from both a reduced Cu matrix grain size and a smaller Ta particle size, the combined strengthening observed from Ta can be almost three times that predicted by Hall–Petch hardening alone (see Fig. 12). The plot, compiled from several sources [61], clearly shows that Cu–Ta alloys deviate dramatically from the expected Hall–Petch trends for pure Cu. In fact, the properties are so extreme that they are more akin to those properties observed for pure nanocrystalline/ultrafine-grained Ta. While the Ta particle dispersion volume fraction plays an important role in defining the yield and ultimate strength values of the Cu matrix, it does not alter the activation volume compared to pure nanocrystalline Cu with similar grain sizes. The measured activation volume of about $50b^3$ is consistent with a dislocation-mediated deformation mechanism. The implication of this result is that controlled decomposition of a forced solid solution between immiscible elements to produce a nanostructured material is a highly effective way to increase the strength of a material well above conventional means provided by grain-size reduction without any significant loss of ductility.

Acknowledgements

The authors extend their thanks to Anthony Roberts for his assistance in the mechanical alloying of the Cu–Ta powder mixtures and Micah Gallagher and David Runk for the ECAE processing of the specimens.

References

[1] Ozerinc S, Tai KP, Vo NQ, Bellon P, Averback RS, King WP. Scr Mater 2012;67:720.
[2] Vo NQ, Chee SW, Schwen D, Zhang XA, Bellon P, Averback RS. Scr Mater 2010;63:929.
[3] Zhang X, Wen JG, Bellon P, Averback RS. Acta Mater 2013;61:2004.
[4] Arshad SN, Lach TG, Pouryazdan M, Hahn H, Bellon P, Dillon SJ, et al. Scr Mater 2013;68:215.
[5] Darling KA, Roberts AJ, Mishin Y, Mathaudhu SN, Kecskes LJ. J Alloys Compd 2013;573:142.
[6] Mula S, Bahmanpour H, Mal S, Kang PC, Atwater M, Jian W, et al. Mater Sci Eng A Struct Mater Prop Microstruct Process 2012;539:330.
[7] Sheibani S, Heshmati-Manesh S, Ataie A. J Alloys Compd 2010;495:59.
[8] Vo NQ, Schafer J, Averback RS, Albe K, Ashkenazy Y, Bellon P. Scr Mater 2011;65:660.
[9] Frolov T, Darling KA, Kecskes LJ, Mishin Y. Acta Mater 2012;60:2158.
[10] Uchic MD, Dimiduk DM, Florando JN, Nix WD. Science 2004;305:986.
[11] Suryanarayana C. Prog Mater Sci 2001;46:1.
[12] Ma E, Atzmon M. Mater Chem Phys 1995;39:249.
[13] Klassen T, Herr U, Averback RS. Acta Mater 1997;45:2921.
[14] Koch CC. Nanostruct Mater 1993;2:109.
[15] Koch CC. Nanostruct Mater 1997;9:13.
[16] Atwater MA, Roy D, Darling KA, Butler BG, Scattergood RO, Koch CC. Mater Sci Eng A Struct Mater Prop Microstruct Process 2012;558:226.
[17] Atwater MA, Scattergood RO, Koch CC. Mater Sci Eng A Struct Mater Prop Microstruct Process 2013;559:250.
[18] Botcharova E, Freudenberger J, Schultz L. Acta Mater 2006;54:3333.
[19] Segal VM. Mater Sci Eng A 1995;197:157.
[20] Furukawa M, Horita Z, Nemoto M, Langdon TG. J Mater Sci 2001;36:2835.
[21] Segal VM. Mater Sci Eng A 1999;271:322.
[22] Valiev RZ, Langdon TG. Prog Mater Sci 2006;51:881.
[23] Zhu YT, Lowe TC. Mater Sci Eng A 2000;291:46.
[24] Haouaoui M, Karaman I, Maier HJ, Hartwig KT. Metall Mater Trans A 2004;35:2935.
[25] Senkov ON, Senkova SV, Scott JM, Miracle DB. Mater Sci Eng A Struct Mater Prop Microstruct Process 2005;393:12.
[26] Robertson J, Im JT, Karaman I, Hartwig KT, Anderson IE. J Non-Cryst Solids 2003;317:144.
[27] Guduru RK, Darling KA, Kishore R, Scattergood RO, Koch CC, Murty KL. Mater Sci Eng A Struct Mater Prop Microstruct Process 2005;395:307.
[28] Guduru RK, Nagasekhar AV, Scattergood RO, Koch CC, Murty KL. Metall Mater Trans A Phys Metall Mater Sci 2006;37A:1477.
[29] Guduru RK, Darling KA, Scattergood RO, Koch CC, Murty KL. J Mater Sci 2007;42:5581.
[30] Guduru RK, Wong PZ, Darling KA, Koch CC, Murty KL, Scattergood RO. Adv Eng Mater 2007;9:855.
[31] Wei Q. J Mater Sci 2007;42:1709.
[32] Chen J, Lu L, Lu K. Scr Mater 2006;54:1913.
[33] Dieter GE. Mechanical metallurgy. New York: McGraw-Hill; 1986.
[34] Meyers MA, Mishra A, Benson DJ. Prog Mater Sci 2006;51:427.
[35] Ramesh KT. Nanomaterials mechanics and mechanisms. New York: Springer; 2009.
[36] Koch CC, Ovid'ko IA, Seal S, Veprek S. Structural nanocrystalline materials fundamentals and applications. Cambridge: Cambridge University Press; 2007.
[37] Li JCM. Mechanical properties of nanocrystalline materials. Singapore: Pan Stanford Publishing; 2011.
[38] Wei QM, Kecskes LJ. In: Li JCM, editor. Mechanical properties of nanocrystalline materials. Singapore: Pan Stanford Publishing; 2011. p. 213.
[39] Chen WN, Song B. Split Hopkinson (Kolsky) bar. New York: Springer; 2011.
[40] Follansbee PS. ASM metals handbook, vol. 8. Materials Park, OH: ASM International; 1985. p. 190.
[41] Nemat-Nasser S. In: Kuhn H, Medlin D, editors. ASM handbook, vol. 8. Materials Park, OH: ASM International; 2007. p. 425.
[42] Wei Q, Kecskes LJ. Mater Sci Eng A 2008;491:62.
[43] Benjamin JS. Metall Trans 1970;1:2943.
[44] Decker RF. Metall Trans 1973;4:2495.
[45] Darling KA, Roberts AJ, Armstrong L, Kapoor D, Tschopp MA, Kecskes LJ, et al. Mater Sci Eng A Struct Mater Prop Microstruct Process 2014;589:57.
[46] Rajulapati KV, Scattergood RO, Murty KL, Horita Z, Langdon TG, Koch CC. Metall Mater Trans A 2008;39:2528.
[47] Guduru RK, Scattergood RO, Koch CC, Murty KL, Guruswamy S, McCarter MK. Scr Mater 2006;54:1879.
[48] Asaro RJ, Suresh S. Acta Mater 2005;53:3369.
[49] Conrad H. Mater Sci Eng A 2003;341:216.
[50] Wu XL, Zhu YT, Wei YG, Wei Q. Phys Rev Lett 2009;103: 205504.
[51] Guduru RK, Murty KL, Youssef KM, Scattergood RO, Koch CC. Mater Sci Eng A Struct Mater Prop Microstruct Process 2007; 463:14.
[52] Wang J, Zhou N, Zhao Z. Adv Mater Res 2011;150 151:1530.
[53] Farrokh B, Khan AS. Int J Plast 2009;25:715.
[54] Suo T, Li Y, Zhao F, Fan X, Guo W. Mech Mater 2013;61:1.
[55] Suo T, Li Y-L, Xie K, Zhao F, Zhang K-S, Deng Q. Mech Mater 2011;43:111.
[56] Wei Q, Pan ZL, Wu XL, Schuster BE, Kecskes LJ, Valiev RZ. Acta Mater 2011;59:2423.
[57] Wei Q, Schuster BE, Mathaudhu SN, Hartwig KT, Kecskes LJ, Dowding RJ, et al. Mater Sci Eng A 2008;493:58.
[58] Taylor GI, Quinney H. Proc R Soc Lond A 1934;143:307.
[59] Caillard D, Martin JL. Therm Activated Mech Cryst Plast. New York: Elsevier; 2003.
[60] Wang YM, Hamza AV, Ma E. Appl Phys Lett 2005;86:241917.
[61] Tschopp MA, Murdoch HA, Kecskes LJ, Darling KA. JOM 2014 (in press), http://dx.doi.org/10.1007/s11837-014-0978-z.
[62] Friedel J. In: Argon AS, editor. Physics of strength and plasticity. Cambridge, MA: MIT Press; 1969. p. 181.
[63] Hashibon A, Elsasser C, Mishin Y, Gumbsch P. Phys Rev B 2007:76.
[64] Seah MP. J Phys F Met Phys 1980;10:1043.
[65] Fu HH, Benson DJ, Meyers MA. Acta Mater 2001;49:2567.
[66] Rigsbee JM. Mater Sci Forum 2007;561 565:2373.
[67] Taylor G. Prog Mater Sci 1992;36:29.
[68] Conrad H. In: Zackey VF, editor. High-strength materials. New York: Wiley; 1965. p. 436.
[69] Carreker Jr RP, Hibbard Jr WR. Acta Metall 1953;1:657.
[70] Lu L, Li SX, Lu K. Scr Mater 2001;45:1163.
[71] Wei Q, Jiao T, Ramesh KT, Ma E, Kecskes LJ, Magness L, et al. Acta Mater 2006;54:77.
[72] Wei Q, Zhang H, Schuster BE, Ramesh KT, Valiev RZ, Kecskes LJ, et al. Acta Mater 2006;54:4079.
[73] Wei Q, Kecskes LJ, Jiao T, Hartwig KT, Ramesh KT, Ma E. Acta Mater 2004;52:1859.
[74] Jia D, Ramesh KT, Ma E. Acta Mater 2003;51:3495.
[75] Grady DE. J Mech Phys Solids 1992;40:1197.
[76] Grady DE. Mech Mater 1994;17:289.
[77] Joshi SP, Ramesh KT. Phys Rev Lett 2008;101:025501.
[78] Guo YZ, Li YL, Pan Z, Zhou FH, Wei Q. Mech Mater 2010;42:1020.